BRNO UNIVERSITY OF TECHNOLOGY

Faculty of Mechanical Engineering

BACHELOR'S THESIS

Brno, 2019 Mgr. Peter Kepič

BRNO UNIVERSITY OF TECHNOLOGY
VYSOKÉ UČENÍ TECHNICKÉ V BRNĚ

FACULTY OF MECHANICAL ENGINEERING
FAKULTA STROJNÍHO INŽENÝRSTVÍ

INSTITUTE OF PHYSICAL ENGINEERING
ÚSTAV FYZIKÁLNÍHO INŽENÝRSTVÍ

ARRAYS OF PLASMONIC NANOSTRUCTURES MADE OF PHASE-CHANGE MATERIALS
POLE PLAZMONICKÝCH NANOSTRUKTUR TVOŘENÝCH MATERIÁLY S FÁZOVOU PŘEMĚNOU

BACHELOR'S THESIS
BAKALÁŘSKÁ PRÁCE

AUTHOR
AUTOR PRÁCE
Mgr. Peter Kepič

SUPERVISOR
VEDOUCÍ PRÁCE
Ing. Filip Ligmajer, Ph.D.

BRNO 2019

VYSOKÉ UČENÍ TECHNICKÉ V BRNĚ
FAKULTA STROJNÍHO INŽENÝRSTVÍ

Zadání bakalářské práce

Ústav:	Ústav fyzikálního inženýrství
Student:	**Mgr. Peter Kepič**
Studijní program:	Aplikované vědy v inženýrství
Studijní obor:	Fyzikální inženýrství a nanotechnologie
Vedoucí práce:	**Ing. Filip Ligmajer, Ph.D.**
Akademický rok:	2018/19

Ředitel ústavu Vám v souladu se zákonem č.111/1998 o vysokých školách a se Studijním a zkušebním řádem VUT v Brně určuje následující téma bakalářské práce:

Pole plazmonických nanostruktur tvořených materiály s fázovou přeměnou

Stručná charakteristika problematiky úkolu:

Na kovových nanostrukturách může díky vysoké koncentraci volných elektronů docházet k plazmonové rezonanci a mohou proto výrazně ovlivňovat chování světla. Toho se využívá např. v nanofotonice, fotovoltaice, magneto–optice nebo při detekci biomolekul. Materiály s fázovou přeměnou do plazmoniky vnáší zejména možnost aktivní laditelnosti a spínání těchto rezonancí. Tato bakalářská práce se bude zabývat optickými vlastnostmi nanostruktur z materiálů s fázovou přeměnou, jako je oxid vanadičitý nebo slitina železa a rhodia. Hlavními úkoly bude vyrábět pole těchto nanostruktur, provádět jejich charakterizaci a studovat, jak souvisí jejich morfologie s optickými vlastnostmi.

Cíle bakalářské práce:

1. Výroba polí kovových nanostruktur z drahých kovů a z materiálů s fázovou přeměnou pomocí elektronové litografie.
2. Ověření vlivu rozměrů nanostruktur a jejich vzájemné vzdálenosti v rámci polí na výsledné optické vlastnosti.
3. Testování vlivu fázové přeměny na plazmonické rezonance a naopak.

Seznam doporučené literatury:

LIGMAJER, F. Advanced plasmonic materials for metasurfaces and photochemistry. Brno: VUT v Brně, CEITEC, 2018.

KRAVETS, V. G., et al. Plasmonic Surface Lattice Resonances: A Review of Properties and Applications. Chem. Rev. 118 (12), s. 5912, 2018.

UHLÍŘ, V., et al. Colossal magnetic phase transition asymmetry in mesoscale FeRh stripes. Nat. Comm. 7, s. 13113, 2016.

Termín odevzdání bakalářské práce je stanoven časovým plánem akademického roku 2018/19

V Brně, dne

L. S.

prof. RNDr. Tomáš Šikola, CSc. ředitel ústavu	doc. Ing. Jaroslav Katolický, Ph.D. děkan fakulty

Abstract

The crystal structure of phase-change materials can be reconfigured by external stimuli, which often result in a change of materials electrical or magnetic properties. Although this effect has been already used to modulate plasmonic resonances in nanophotonics, it has not been fully examined for the two materials chosen in this work — vanadium dioxide (VO_2) and iron-rhodium alloy (FeRh). Plasmonic resonances can be described as resonances of electromagnetic field in metallic nanostructures. With these nanostructures we are even able to modulate light. In this thesis, we firstly optimized electron beam lithography process for production of metal nanodiscs with 40–200 nm diameters. Secondly, we measured an optical response of gold nanodiscs to better understand the nature of their plasmonic resonances and interactions between them. Lastly, we described the optimization of polycrystalline VO_2 growth and measured optical responses of VO_2 and FeRh nanodiscs during their respective phase transitions. Our observation of Mie's resonances in the dielectric phase of the VO_2 nanodiscs suggests, that they have a potential to act as tunable plasmonic resonators which switch from Mie's resonances in the dielectric phase into plasmonic resonances in the metallic one. When measuring the FeRh nanodiscs, we observed plasmonic resonances in the visible part of the spectrum. These resonances can be used to facilitate FeRh transition from an anti-ferromagnetic to a ferromagnetic phase, as they could lower the required latent heat.

Keywords

nanodiscs, plasmonics, electron beam litography, phase-change materials, tunable plasmonic resonances, vanadium dioxide, iron-rhodium alloy

Abstrakt

Kryštálovú štruktúru materiálov s fázovou premenou dokážeme meniť dodaním vonkajšej energie, čo má za následok zmenu ich elektrických alebo magnetických vlastností. Hoci sa tento efekt ovládania plazmonických rezonancií v nanofotonike využíva, dva materiály zvolené v tejto práci — oxid vanadičitý (VO_2) a zliatina železa a ródia (FeRh) — neboli zatiaľ dostatočne preskúmané. Plazmonické rezonancie môžu byť charakterizované ako rezonancie electromagnetického poľa v kovovvých nanoštruktúrach. Týmito nanoštruktúrami sme dokonca schopní ovládať svetlo. Na začiatku tejto práce sa venujeme optimalizovaniu procesu elektrónovej litografie pre výrobu 50 nm vysokých kovových nanodiskov s priemermi 40–200 nm. V druhej časti skúmame optickú odozvu zlatých nanodiskov, aby sme lepšie pochopili povahu plazmonických rezonancií a interakcií medzi nimi. V poslednej časti sa venujeme optimalizácii výroby polykryštalického VO_2 a meraniam optických odoziev VO_2 a FeRh nanodiskov počas ich fázovej premeny. Pri meraní VO_2 nanodiskov v dielektrickej fázi sme pozorovali Mieho rezonancie. Tieto nanodisky sa majú potenciál chovať ako laditeľné plazmonické štruktúry, ktorých Mieho rezonancie v dielektrickej fázy VO_2 sa menia na plazmonické rezonancie v kovovej fázy. Počas merania FeRh nanodiskov sme pozorovali plazmonické rezonancie vo viditeľnom spektre. Tieto rezonancie môžu byť použité na zníženie energie potrebnej na prechod FeRh z anti-feromagnetickej do feromagnetickej fázy.

Klíčová slova

nanodisky, plazmonika, elektrónová litografia, materiály s fázovou premenou, laditeľné plazmonové rezonancie, oxid vanadičitý, zliatina železa a ródia

KEPIČ, P. *Pole plazmonických nanostruktur tvořených materiály s fázovou přeměnou.* Brno: Vysoké učení technické v Brně, Fakulta strojního inženýrství, 2019. 47 s. Vedoucí práce Ing. Filip Ligmajer. Ph.D.

Prehlasujem, že som predloženú bakalársku prácu s názvom "Pole plazmonických nanostruktur tvořených materiály s fázovou přeměnou" vypracoval samostatne pod vedením Ing. Filipa Ligmajera, Ph.D, a že všetky podklady, z ktorých som čerpal, uvádzam v priloženom zozname použitej literatúry.

Mgr. Peter Kepič

Týmto by som chcel poďakovať Ing. Filipovi Ligmajerovi, Ph.D. za jeho odborné vedenie a ochotu vždy pomôcť s nejasnosťami vzniknutými pri výrobe vzoriek, meraní vzoriek a interpretácií výsledkov. Obzvlášť ďakujem za jeho trpezlivosť pri opravovaní a konzultovaní mojej bakalárskej práce. Zároveň by som sa chcel poďakovať doc. Ing. Radkovi Kalouskovi, Ph.D. za odborné rady v teórii plazmoniky a teoretický model, Ing. Jiřímu Babockému, Ing. Vojtěchovi Švarcovi a Mgr. Jiřímu Liškovi, Ph.D. za odborné rady k elektrónovej mikroskopii, M.Sc. Jon Ander Arregimu za depozíciu zliatiny železa a ródia a Janovi Hajdučkovi za výrobu nanodiskov zo zliatiny železa a ródia. V neposlednej rade by som sa rád poďakoval svojej rodine, spolužiakom a obzvlášť svojej snúbenici Lili za psychickú podporu a trpezlivosť počas písania mojej bakalárskej práce.

Výroba a následná analýza vzoriek bola vykonaná za podpory výskumnej infraštruktúry CEITEC Nano (ID LM2015041, MŠMT, 2016–2019), CEITEC Vysoké učení technické v Brně.

Mgr. Peter Kepič

Contents

Introduction

The field of plasmonics, the science of light–metal interactions, has been studied already for at last two decades. Plasmonics has found applications in many areas, such as solar cells, or subwavelength imaging, where the control of light plays the key role. One of the ways how to control light is to create nanostructures from materials with a phase transition. In some materials, this transition is responsible for significant changes of electrical or magnetic properties, and can be triggered by external stimuli, such as heat, electricity, or strain. Thus, in plasmonic nanostructures, the transition can work as a switch that alters the light on demand. This behavior can be also used in reverse, when the plasmonic nanostructures facilitate the phase transition as they supply a part of the required energy.

One of the materials with such a phase transition is vanadium dioxide (VO_2). Even though VO_2 nanostructures have been studied, a combination of Mie's dielectric resonances with plasmonic resonances in phase-changing VO_2 nanostructures have not been examined yet. A similar thing can be said about another phase-change material — iron-rhodium alloy (FeRh). The optical response of FeRh nanostructures and applications of its plasmonic resonances on lowering the energy required for the transition have not been studied at all.

Chapter 1 starts with a description of various nanofabrication methods and compares their advantages and drawbacks. It focuses mostly on EBL — the method used in this thesis. We describe optimization of the EBL process for the production of 50 nm high nanodiscs with 40–200 nm diameters. The chapter finishes with a detailed recipe, which can serve as guidelines for nanodiscs production made of various materials.

Chapter 2 is devoted to plasmonics. It starts with the theory of plasmonics, which should facilitate deeper understanding of the physical nature of plasmonic resonances, which are subsequently observed on nanostructures made of the most common noble metal — gold. The observation is done in the visible part of the spectrum for single gold nanodiscs (GNDs) and GND arrays. The results from measurements and simulations are compared with the theoretical model for the localized surface plasmon resonances (LSPRs). The measurements also reveal what influence the far-field interactions within the array have on the resulting collective LSPRs.

Chapter 3 is centered around phase-change materials — VO_2 and FeRh. After introducing the detailed mechanism of VO_2 transition and its current applications, we move to optimization of growth of polycrystalline VO_2. Out of the optimization process, VO_2 films with the biggest contrast in transmittance during the phase transition are selected for subsequent fabrication of nanodisc arrays. The arrays are measured in the visible part of the spectrum for both phases of VO_2, where resonances in dielectric phase are revealed. After dealing with VO_2, we introduce a detailed mechanism of a FeRh transition and its current applications. Then we measure the optical response of

FeRh nanodiscs. The LSPRs are confirmed for both phases of FeRh, with only up to 30 nm resonant wavelength difference between their peak positions.

Overall, the main goal of this thesis is to provide an overview of plasmonic resonances of Au, VO_2 and FeRh nanodiscs. The understanding of interactions between nanodiscs in arrays and ordering those nanodiscs into a specific lattice can significantly increase the quality factor of the collective nanodisc resonance. Combining resonances of VO_2 nanodiscs in its dielectric phase with plasmonic resonances of VO_2 in its metallic phase can lead to tunable optical elements. The FeRh plasmonic resonances, on the other hand, can facilitate the energy required for the phase transition of FeRh nanostructures. All of those applications are only a small part of what plasmonics, especially plasmonics of the phase-change materials, can bring for the future development in nanotechnology.

1. Nanofabrication

The semiconductor era has been a huge step in human history. It has changed computing possibilities and communication in the way people from the sixties could not imagine. Take for example a transistor — the main component of all electronic devices today. It has shrunk from the millimeter scale to the nanometer scale within 25 years; following the famous Moore's law [1]. The effort to shrink the transistor lead to evolution of the relevant nanofabrication methods, which then opened many new possibilities for science and technology.

Nanofabrication plays a key role in nanotechnology research. To investigate physical phenomena, scientists have to use all sorts of methods to fabricate specific nanostructures. Although those methods are used mostly for basic research, an industry already takes advantage of it [2]. Nanofabrication is thus an example of long-term cooperation, in which improvement, driven by the industry, opens up new possibilities for science, which, by discovering new phenomena, provides new products for that industry in return.

Therefore, in the first chapter, we will shortly describe various nanofabrication methods and compare their advantages and disadvantages in the quality, time consumption and costs. Then, we will select one representative method which is the most relevant to the current work — EBL — and we will describe it in more detailed manner, with emphasis on a detailed description and optimization for nanodiscs production.

1.1 Nanofabrication methods

Nanofabrication is a crucial instrument for nanotechnology. It is a process of fabricating controlled nanostructures (from one to few hundred nanometers). The word "controlled" is important, as the size, shape, and material must precisely match the desired specification. How much it must be controlled depends on the used method.

One of the oldest approaches is the chemical synthesis of colloidal nanoparticles. Spherical nanoparticles with diameters in the range of 2–250 nm can be created simply by mixing chemicals under the certain conditions. Despite possibility to create precise diameters, a disadvantage of the chemical synthesis lies in the complicated precise placement of those particles [3].

This disadvantage of chemically synthesized nanostructures can be mitigated by a dip-pen lithography. It is a scanning probe technique, that requires an atomic force microscope (AFM), where a scanning tip is coated with the solution of interest. Due to humidity, a water meniscus between the probe and the substrate is created, which enables diffusion of molecules onto the substrate (see Figure 1.1a). That way, organic

molecules or gold atoms can be patterned with a resolution down to 5 nm [4, 5]. Local anodic oxidation is another scanning probe method. It also requires the water meniscus between the AFM tip and the substrate, but instead of molecules diffusion, high voltage is applied between the tip and the substrate. This voltage dissociates molecules of water into hydrogen and oxygen atoms, where the latter one subsequently reacts with the substrate and oxidizes it (see Figure 1.1b). The advantage lies in the precise oxidized structures, that depends on the tip, substrate and humidity. The precision of both methods is compensated with long fabrication time [6].

Another class of methods is a focused electron/ion beam induced deposition/etching (FEBID/FIBID/FEBIE/FIBIE). It combines an electron, or ion beam microscope with a gas injection system (GIS). The main component of this system is a hollow micro-tube, which injects molecules of the specific gas on top of the substrate. Injected molecules of gas are dissolved by the beam. Based on a type of gas, dissolved molecules either etch, or, conversely, are deposited onto the substrate (see Figure 1.1e). Besides the possibility of local etching, or faster structuring than scanning probe methods, the biggest GIS advantage is the deposition of the particular group of materials [7, 8]. However, it is still quite slow method compare to others.

The most used method in the industry is photolithography. It uses photons to expose a thin layer of the material (called photo-resist), reactive to photons, through a mask. The exposed places of the photo-resist are dissolved in the special liquid developer and used as the opaque layer for the next deposition or etching step [4]. The mask can be applied in a contact, proximity, or projection mode (see Figure 1.1c), where each has its own pros and cons [9]. The photolithography, compare to other classes of methods, is the fastest method on one hand, with the worst resolution due to a diffraction limit on the other hand. Its use in research is smaller, as the expensive mask, meant for bigger production, is not needed.

Just like the photolithography, electron beam lithography (EBL) uses the layer of the resist as an intermediary for the next deposition or etching step. However, the exposure is done by a focused electron beam instead of photons passing through the mask. Due to scanning, EBL provides a lower throughput, but the resolution can be as high as 5 nm [10]. Within the resolution, it maintains the shortest production time of precise ordered nanostructures, compare to all aforementioned methods. Therefore, EBL is the most used method in the scientific research.

Beside aforementioned methods, there are two other lithographies, that get more attention in the recent years. The first of them is a soft lithography, which is based on stamping a material onto the substrate, through the stamp prepared by EBL. The second one is a nanoimprint lithography. It uses the EBL-prepared mask with a nanometer precision, which molds the specific resist. Using these methods, a large amount of reproducible precise nanostructures with the resolution down to 5 nm would be possible to achieve in the shorter time than EBL [6].

As seen in the previous paragraphs, there is a huge variety of nanofabrication methods. It is the specification of the experiment that ultimately decides, which method is the most suitable one to use. EBL is the best option for a production of ordered metallic or dielectric nanostructures in small arrays. As the production of those arrays is one of the goals of this thesis, we will focus on EBL in detail.

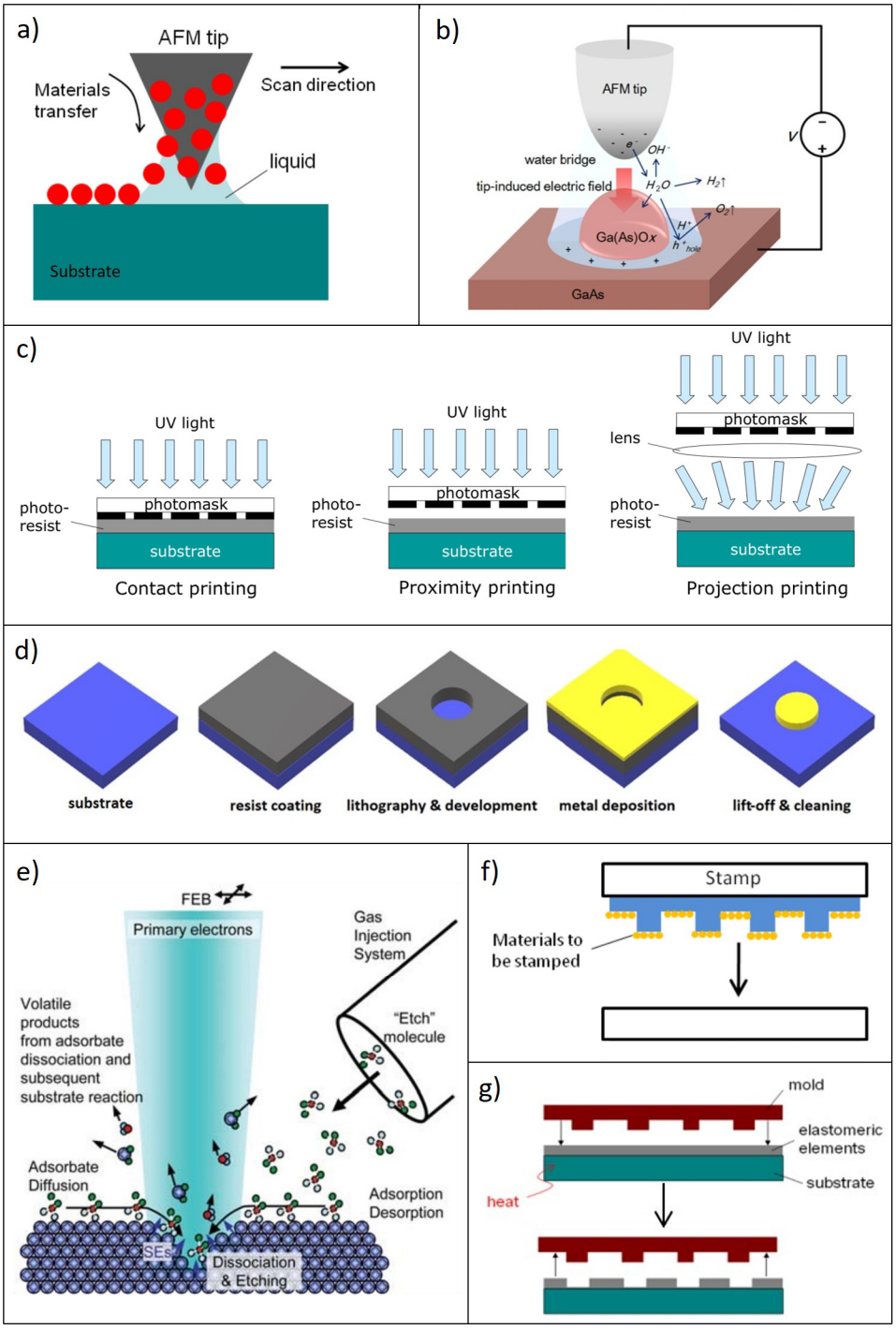

Figure 1.1: Nanofabrication methods: a) Dip-pen lithography — atoms are diffused from the tip onto the substrate through the water meniscus [5]. b) Local anodic oxidation — applied voltage dissociates water into hydrogen and oxygen atoms, where the latter one subsequently oxidizes the substrate underneath [11]. c) Photolithography — three modes, which differ based on a distance of a mask from a substrate. In all cases, UV light exposes a resist on the substrate through opened places in the mask [5]. d) EBL process — covering a substrate with a resist, exposing and developing a desired pattern, a metal deposition and lastly a lift-off, to get rid of the residual resist [12]. e) FEBIE — injected gas is dissolved by the electron beam and etches a substrate [13]. f) Soft lithography — a nano-stamp is covered with a material, which is afterward stamped onto the substrate [5]. g) Nanoimprint lithography — a mold is pressed into a moldable resist, which reproduces a desired pattern [5].

1.2 Electron beam lithography (EBL)

Comparison of various nanofabrication methods showed, that EBL is the most common way to produce nano-sized metallic or dielectric nanostructures in specific patterns. A basic EBL consists of spin-coating, exposure, development, deposition/etching and lift-off as shown in Figure 1.1d [14–16].

Spin-coating is a process of covering the substrate with a resist. It starts with cleaning the substrate with acetone, isopropyl alcohol (IPA), water and pre-baking. The reason is to get rid of unwanted particles on the substrate. After the cleaning, the resist is applied on top of the substrate by a pipette in the form of a droplet. When the sample is spanned between 2000–7000 rpm, the droplet spreads and covers the whole substrate equally. The covered sample is hard-baked at the end (Figure 1.2).

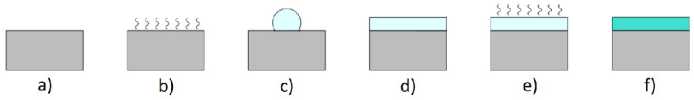

Figure 1.2: Spin-coating: a) the cleaned substrate, b) pre-bake, c) the resist applied in the form of a droplet, d) the resist equally spanned, e) hard-bake, f) the sample is ready for exposure [16].

Exposure is the crucial part of the whole EBL process. It is the part with the most parameters, which influences a successful fabrication. The sample is put into Scanning electron microscope (SEM) or a specialized electron beam lithographic apparatus. After the electron beam is focused and parameters (specific for the used machine) set, the pattern from a computer is exposed onto the sample. As there are two types of the resist, two types of results can be achieved. For a positive one, an interaction between electron beam and the resist causes a chain scission of molecules, making it possible to dissolve patterned places in a developer solution. For a negative one, on the other hand, molecules are cross-linked. The developer solution sweeps away everything beside those nanostructures. The quality of development is influenced by the time spent in the developing bath.

When the development is successful, the sample can be covered with a metallic or dielectric material by various deposition techniques, for example, a physical or chemical vapor deposition, or magnetron sputtering [14]. The other option after the development, is a dry (with ions) or wet (with chemicals) etching. If the experiment requires to create nanostructures out of the material, deposited before the exposure, etching and the negative resist are mostly implied. In case, the material is deposited after the development, the positive resist and deposition are incorporated.

Lift-off is the last step of the EBL. The residual resist (under the deposited layer) is cleared away by the specific liquid removal, or etched in O_2 plasma. In the case of liquid removal, if the material still stays on the substrate, an ultrasound treatment can be applied.

Having a detailed recipe for the EBL will not guarantee successful fabrication. Each project has its own specification, that is why we will focus on optimization of EBL for our specific plasmonic nanostructures — nanodiscs.

1.3 EBL nanodiscs optimization

The goal of this thesis was to observe plasmonic resonances in gold and materials with a phase transition. To avoid dealing with polarization of the incident electromagnetic wave, we decided to focus on nanodiscs, due to their rotational symmetry. As nanodiscs were expected to reveal an interesting behavior at short wavelength [17], we wanted to produce nanodiscs as small as possible. Therefore, optimization of the EBL was done for GNDs with 40, 80 and 200 nm diameters on a conductive silicon substrate (Si).

Optimization started with laser-cutting a 2 inch diameter silicon wafer from the company Siegert wafer GmbH into 10×10 mm sized samples. Four cut samples were cleaned for 2 min in acetone bath (using ultrasound), then in IPA for 2 min, deionized water for 30 s and baked for 2 min on a 100 °C hotplate. After that, they were spin-coated on the Süss Microtec lithographic wet bench at 4000 rpm with a CSAR 6200.07 and CSAR 6200.09 — positive resists from the Allresist company. Their difference is in the thickness of the layer, where the CSAR 6200.09 is thicker than the CSAR 6200.07. For the exposure, we used the SEM Tescan MIRA3, which is upgraded with the Elphy plus software from Raith nanofabrication company for lithographic purposes. With samples inside the SEM, we aligned an electron beam column for 30 kV voltage and 2 different currents, 25 pA and 47 pA. This manual [18] describes the aligning procedure step by step. After the electron beam alignment, we adjusted the Elphy plus software, following the user manual [19]: choosing origin, aligning software, three points working distance adjustment (so the sample is always focused), choosing write-field, and patterning parameters. Patterning parameters include a settling time, patterning mode, step size and area dose. Settling time is the time allowed for a beam to become stationary at a new location [19]. Changing an automatic settling time causes prolongation, but no improvement in a quality. The patterning mode means a different path of the exposure. It is divided into many types (see again [19]), but we decided to work with the line (meander) scan and concentric (clockwise) scan. Meander scan represents scanning in a line without stopping, that means, if the beam comes from the left and reaches the edge of the structure, it jumps one line up and continues patterning backward. For a concentric scan, the beam follows an inward spiral movement, which copies the shape of the structure. The last thing we did, before engaging the exposure, was to set a dose. It describes a dose in coulombs exposed on a squared centimeters and can be calculated as [19]

$$D = \frac{I_B}{l_S} t_D, \tag{1.1}$$

where I_B is the beam current, l_S the step size (set to 5 nm) and t_D is the dwell time.

The goal of the optimization was to test an influence of 4 above-mentioned parameters on the exposure time, quality and size of nanodiscs. We tested two resists — CSAR 6200.07 and CSAR 6200.09, two currents — 25 pA and 47 pA, two patterning modes — meander and concentric, and six doses from 110 to 160 μC/cm^2 for nanodisc arrays of three different diameters. In this section we will focus only on 40 nm and 200 nm, as results for 80 nm nanodiscs show almost the same behaviour as results for 200 nm nanodiscs.

Firstly, we started with the comparison of the meander and concentric scan. As there was no difference in accuracy of target nanodisc sizes and quality of the resulting nanostructures, we decided to continue with the concentric scan.

Secondly, we compared doses for both resists and currents. Taking for example 40 nm nanodiscs, created with CSAR 6200.07, 25 pA and lower doses, they were not even patterned, as shown in Figure 1.3. For the 160 μC/cm^2 dose, the success of fabrication got above 95 %. For bigger nanodiscs, the success has been achieved for all doses, just the accuracy of sizes and quality varied (see Table 1.1).

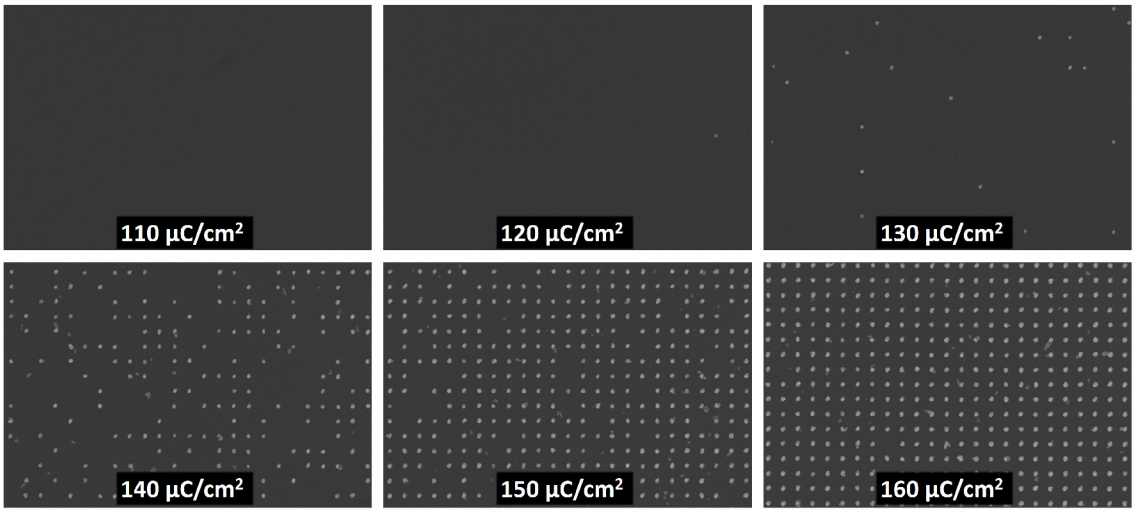

Figure 1.3: SEM micrograph of the 40 nm GND arrays resulting from EBL process with CSAR 6200.07 and 25 pA, but varying dose factor (see labels).

Thirdly, we took SEM micrographs of the most successfully patterned 40 nm nanodisc arrays for the each resist and current and compared the success and precision of nanofabricated nanostructures. As we can see in Figure 1.4, exposing CSAR 6200.07 with 25 pA seems to give the most promising result. The higher dose could increase the success in thicker CSAR 6200.09, but it would result in bigger diameters (see Table 1.1).

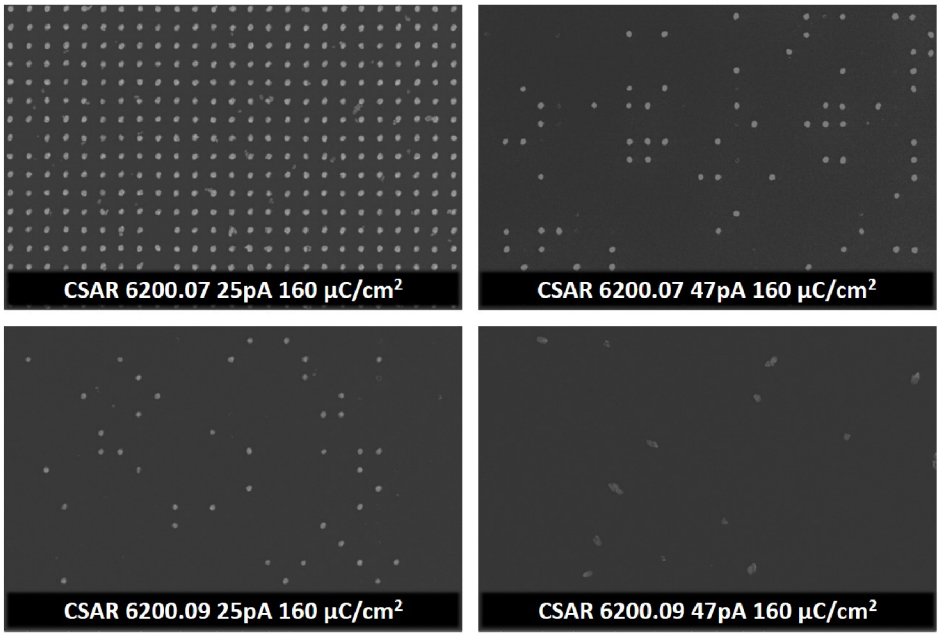

Figure 1.4: SEM micrograph of the 40 nm GND arrays resulting from EBL process with parameters described in labels.

So far, we focused only on the qualitative aspect of our EBL. For the quantitative aspect we measured nanodisc diameters from SEM micrographs of the each array by Gwyddion analysis software. A comparison of the actual diameters in Table 1.1 reveals, that doses for bigger diameter nanodiscs need to be different than for smaller ones. The comparison also reveals better results when CSAR 6200.07 is used. Combining qualitative and quantitative results, we can come up with detailed guidelines for the EBL of nanodiscs.

Table 1.1: Diameters (in nanometers), as measured from SEM micrographs of the resulting nanodiscs, for different combinations of dose factor, resist type, beam current and target size. Places in the table without a number represents unsuccessful fabrication.

Dose Factor [μC/cm^2]	CSAR 6200.07				CSAR 6200.09			
	25 pA		47 pA		25 pA		47 pA	
	40 nm	200 nm	40 nm	200 nm	40 nm	200 nm	40 nm	200 nm
	D [nm]							
110	-	197	-	192	-	188	-	184
120	-	200	36	195	-	194	-	193
130	30	203	39	201	-	200	-	199
140	39	207	41	203	-	203	-	208
150	40	210	43	208	-	206	-	206
160	43	212	45	210	35	210	-	211

To conclude this section, we optimized EBL for 40 , 80 and 200 nm nanodiscs. The goal was to get the most accurate size and shape, while keeping the shortest time of exposure as possible. For that, we tested 4 parameters: the scan mode, dose, type of the resist and current.

For 40 nm nanodiscs, we suggest to use the 30 kV, 25 pA, 5 nm step size, concentric mode, automatic settling time and 160 μC/cm^2, while using CSAR 6200.07. For bigger nanodiscs, conditions would be the same, as it is usually produced on the same sample in a one exposure round. So the only difference is the area dose, which would be 130 μC/cm^2. The area dose can be easily adapted in the software, based on the size of the exposed structure.

This chapter reviewed different types of nanofabrication methods, out of which the EBL came out like the best one for the production of the specific plasmonic nanostructures that will be studied in this work. The chapter was meant to provide a detailed technical guide for the EBL, which was optimized for plasmonic nanodiscs production, using gold on a silicon substrate. The next chapter moves on to discuss the field of plasmonics and the measurement of plasmonic resonances in gold nanodiscs.

2. Plasmonics

The first systematic studies of the interaction between an electromagnetic wave and a metal surface were reported by A. Sommerfeld in 1899 [20] and P. Drude in 1900 [21]. Followed by J. Zenneck's article about radiowave propagation on the metal surface in 1907 [22], the beginning of the 20th century was a dawn of a new field called plasmonics. Although it has started more than 100 years ago, the concept was theoretical at first. Due to technological possibilities, plasmonics could be verified experimentally only in the last 20 years.

The aforementioned interaction creates light-matter oscillations, represented by quasi-particles called plasmon polaritons, or shortly plasmons. They have an ability to focus light under the diffraction limit. When the metal surface is spatially restricted, plasmons become localized and their properties become easier to control. Thus, those controlled properties can be adopted into a variety of applications. For example the localized focusing below the diffraction limit can improve photovoltaics [23–26] and photodetection [27–30]. Due to absorption of the restricted metal nanostructures, the focusing can be used also for nanoscale local heating [31–34]. Using a property of changing a phase of the wave, nanostructures can be assembled into artificial materials (surfaces), called metamaterials (metasurfaces), capable of even redirecting electromagnetic waves [35–41]. Beside the aforementioned applications, plasmonics can be used also in biochemistry for sensing [3, 42–44].

As documented by the number of articles on the topic and also by their publication dates, there is a growing interest in plasmonics these days. Most of the research done in articles require a proper fabrication and a full understanding of the above-mentioned subject. Therefore, in this chapter, we will briefly discuss a theory of plasmonics, focusing on plasmonic antennas, and look closer on a difference between resonances of a single GND and GND array.

2.1 From plasmonics to localized surface plasmon resonances

When we talk about the interaction between an electromagnetic wave (further denoted only as the wave) and a metal surface (further denoted only as the surface), we work with electromagnetism and solid state physics. Plasmonics incorporates those two fields. When the wave impinges on the surface, it forces free (in case of metals) or even bounded (in case of dielectrics) electrons to oscillate in a direction of the electric field. To describe their behaviour and come up with dielectric function that defines optical response of the material, we can use Drude's model [45] that approximates an electron in the metal as a free harmonic oscillator. This way we come up with the dielectric

function for metals

$$\varepsilon(\omega) = 1 - \frac{\omega_{\mathrm{p}}^2}{\omega^2 + \mathrm{i}\gamma\omega}, \tag{2.1}$$

where γ is the damping coefficient and ω_{p} is the plasmon frequency of the metal. The dielectric function is a complex function, which real part can acquire negative values.

The previous equation describes optical response of the metal. To understand the interaction between the surface and wave more, we must solve Maxwell's equations [46] on the boundary between the metal and surrounding environment. The solution introduces a new quasi-particle called plasmon polariton, or shortly plasmon. This particle represents light-matter oscillations, which propagate on the surface with the wave number [45]

$$\beta(\omega) = k_0(\omega)\sqrt{\frac{\varepsilon_{\mathrm{d}}(\omega)\varepsilon_{\mathrm{m}}(\omega)}{\varepsilon_{\mathrm{d}}(\omega) + \varepsilon_{\mathrm{m}}(\omega)}}, \tag{2.2}$$

where k_0 is the wave number of the incident wave, ε_{d} and ε_{m} are dielectric functions of the surrounding environment and metal, respectively. Implementing Eq. (2.1), we find out that β can acquire values larger than k_0 for the specific frequencies, hence the wavelength of plasmon can be smaller than wavelength of the incident light. This proves the focusing ability of plasmons.

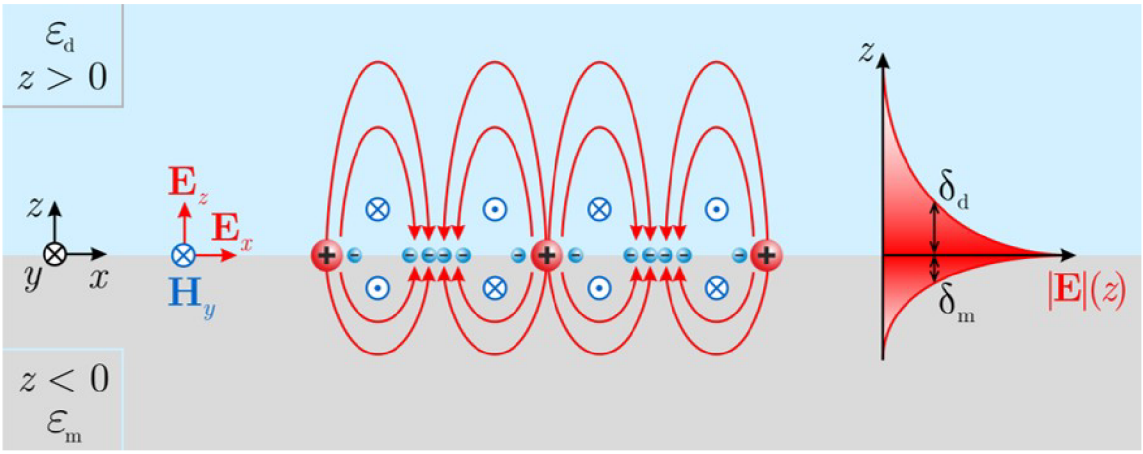

Figure 2.1: Illustration of the field distribution for surface plasmon polaritons. Electrons (blue minuses) oscillate around cores (red pluses), while give rise to the electric field in xz plane (red lines) and the magnetic field along y axis (blue marks). The right part of the picture represents penetration depth, where δ_{d} and δ_{m} are penetration coefficients. Adapted from [47].

Now, when we defined surface plasmon polaritons, let us look closer on their localized version. Localized surface plasmons (LSPs) are non-propagating excitations of electrons, which arises from the spatial restriction of the metal part. Therefore, having a certain metal nanoparticle (NP), we can observe LSPs. To understand their nature, we will start with the simple quasi-static approximation of a metal sphere illuminated by an electromagnetic plane wave (see Figure 2.2). This approximation means that a phase of the wave in the sphere can be considered homogeneous. For finding a response of the sphere on the wave we calculate the Laplace equation [46]. While considering

boundary conditions, we obtain relationship for the internal and external electric field [48]

$$\mathbf{E_{in}} = \frac{3\varepsilon_\mathrm{d}}{\varepsilon(\omega) + 2\varepsilon_\mathrm{d}}\mathbf{E}, \tag{2.3}$$

$$\mathbf{E_{out}} = \mathbf{E} + \frac{3\hat{\mathbf{n}}(\hat{\mathbf{n}} \cdot \mathbf{p}) - \mathbf{p}}{4\pi\varepsilon_0\varepsilon_\mathrm{d}}\frac{1}{r^3} \equiv \mathbf{E} + \mathbf{E_{sca}}, \tag{2.4}$$

where $\mathbf{E}$ is the initial electric field, $\hat{\mathbf{n}}$ the unit vector, ε_0 the permittivity of vacuum, r the distance between the particle and a position of interest, and $\mathbf{p}$ is a dipole moment defined as

$$\mathbf{p} = \varepsilon_0\varepsilon_\mathrm{d}4\pi R^3\frac{\varepsilon(\omega) - \varepsilon_\mathrm{d}}{\varepsilon(\omega) + 2\varepsilon_\mathrm{d}}\mathbf{E} = \varepsilon_0\varepsilon_\mathrm{d}\alpha\mathbf{E}, \tag{2.5}$$

where R is the radius of the sphere and α the polarizability.

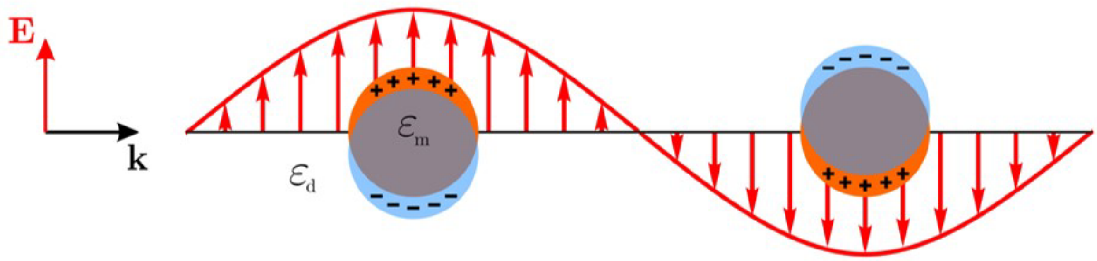

Figure 2.2: Two nanoparticles are illuminated with the plane wave. Electrons (marked as blue) are oscillating up and down, creating positive charges (marked as orange) on the opposite side. Adapted from [47].

Almost all experiments work with an intensity of the wave, so it is more common in plasmonics to work with a scattering and absorption cross-section rather than the electric field. They express ratio between the wattage $P_{\mathrm{sca/abs}}$ scattered/absorbed by the NP and incoming light intensity I_inc. They are defined as [45]

$$C_\mathrm{sca} \equiv \frac{P_\mathrm{sca}}{I_\mathrm{inc}} = \frac{k^4}{6\pi}|\alpha|^2 = \frac{8\pi}{3}k^4R^6\left|\frac{\varepsilon(\omega) - \varepsilon_\mathrm{d}}{\varepsilon(\omega) + 2\varepsilon_\mathrm{d}}\right|^2, \tag{2.6}$$

$$C_\mathrm{abs} \equiv \frac{P_\mathrm{abs}}{I_\mathrm{inc}} = k\mathrm{Im}(\alpha) = 4\pi kR^3\mathrm{Im}\left|\frac{\varepsilon(\omega) - \varepsilon_\mathrm{d}}{\varepsilon(\omega) + 2\varepsilon_\mathrm{d}}\right|. \tag{2.7}$$

For $\varepsilon(\omega) = -2\varepsilon_\mathrm{d}$, the system enters the regime of the localized surface plasmon resonance (LSPR), enhancing the scattering and absorption cross-section. If we would focus on a position of the LSPR, we would find out that for this approximation it stays on the same frequency (or wavelength), no matter a size, shape, or configuration of NPs. To include the size and shape dependence [17, 49–51], and the interaction between particles [52, 53] into the position of the LSPR, we have to use other theoretical models like Mie's theory [54] or free electron gas model [55].

The above-mentioned dependence on the shape, size and configuration of NPs shows why nanofabrication is so important. By precise fabrication of NPs, we can enhance electric field at the specific wavelength. Thus, in most cases we work with the LSPR

wavelength as a function of the size (for the specific shape). This function can be calculated by the free electron gas model. Based on the unpublished work of R. Kalousek, LSPR wavelength for a nanodisc with its diameter much larger than its height can be calculated as

$$\lambda_{\mathrm{LSPR}} = \frac{25.1}{\omega_{\mathrm{eff}}} \frac{cD/2}{h} \frac{1}{\sqrt{\sqrt{1+\frac{D^2}{h^2}}-1}}, \tag{2.8}$$

where c is the speed of light, D the nanodisc diameter, h the height of the nanodisc, and ω_{eff} is the effective plasma frequency expressed as

$$\omega_{\mathrm{eff}} = \sqrt{\frac{ne^2}{\epsilon_0 \epsilon_d m_e}}, \tag{2.9}$$

where n is the density of charge carriers, e the elementary charge, m_e the mass of an electron. This equation shows a root function dependence of LSPR wavelength on the diameter of the nanodisc.

This section has provided a brief summary of plasmonics, focusing on plasmon polaritons and LSPs. The summary resulted in the relationship for the LSPR wavelength as the function of the nanodiscs diameter and height. In the next section we will investigate this theoretical model by measuring the LSPRs of single GNDs. We will also measure the optical response of GND arrays and compare their resonances with the single GNDs measurement.

2.2 Gold nanodiscs measurement

To understand the theory and measuring instrument better, we decided to observe LSPRs for the most common noble metal — gold. Using optimized parameters from the section 1.3, we fabricated 40–200 nm diameter gold nanodiscs, with 50 nm height and 3 nm titanium adhesion layer, on a fused silica (SiO_2) substrate, using the EBL. The gold and titanium were evaporated on the electron beam evaporator Bestec GmbH. Based on Eq. (2.8), LSPRs were expected to be in the visible part of the spectrum. Thus, we decided to measure them with the Andor Shamrock 500i spectrometer from the Oxford instruments company in combination with an optical microscope from the Olympus company.

Previous bright-field (BF) transmittance measurements [17, 50, 56] proved, that nanodiscs arrays on SiO_2 show a clear and strong signal. Thus, we started with a BF transmittance measurement of $100\times100\,\mu$m GND arrays for the above-mentioned diameters, where the distance between the centers (pitch) of nanodiscs was three times their diameter (3d). We used 10× objective Olympus with a numerical aperture (NA) 0.25 as a condenser and also as a collector. An aperture stop (AS), represented by an optical element which cuts outside portion of the incident beam (see Figure 2.3b), reduced the incident beam to its inner-most part. The incident angle distribution was thus limited to values close to 0°, creating the most perpendicular planar wave on the microscope. It was our goal due to a simplicity of a simulation, as a perpendicular (to the surface) planar wave is easier to simulate. The simulation has served as comparison to the measured data and has been done in the Lumerical Finite-Difference Time-Domain (FDTD) software, using periodic boundary conditions.

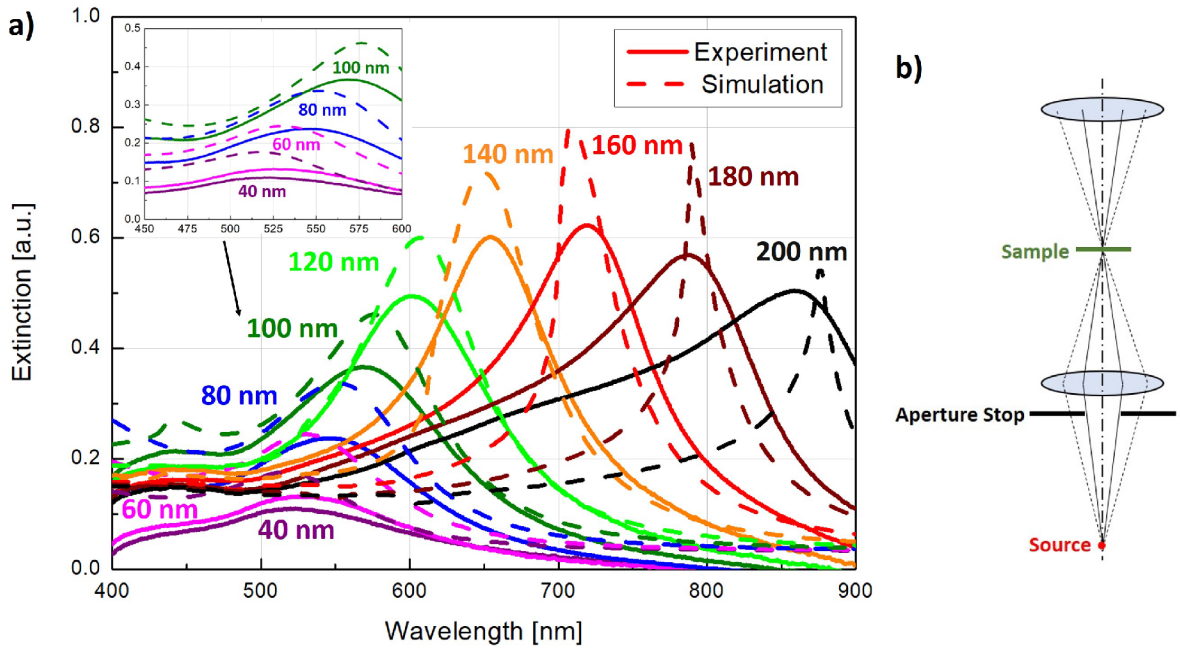

Figure 2.3: a) Experimental and simulated extinction spectra of GND array with 3d pitch and the varying nanodisc diameter. b) Illustration of the aperture stop, which on one hand decrease the light intensity, but on the other hand creates more perpendicular planar wave, by reducing the incident beam to its inner-most part.

The extinction in Figure 2.3a represents a quantity calculated as

$$E = 1 - \frac{I}{I_0}, \tag{2.10}$$

where I is the light intensity transmitted through the array and I_0 is the reference light intensity transmitted through the SiO_2 substrate. The extinction can be also approximately expressed as [51]

$$E \approx NC_{\text{ext}} = N\left(C_{\text{sca}} + C_{\text{abs}}\right), \tag{2.11}$$

where N is the number of measured nanodiscs and C_{ext} is the extinction cross-section. This relationship puts the extinction into a direct proportionality with the scattering cross-section. The experiment and simulation (Figure 2.3a), shows the significant match. The simulated data also exhibit sharpening of the LSPR for bigger diameters of nanodiscs. It happens due to the pitch in the array and the source, illuminating the whole infinite array, created by periodic boundary conditions. This problem will be discussed in later, in comparison of LSPR wavelengths for single GNDs and GND arrays. Experimental data do not indicate such strong sharpening, due to a finitely illuminated part of the array (spot size is a 90 μm diameter circle) and imperfection in the shape of nanodiscs.

Experimenting with the opened and closed aperture stop and varying collecting objectives, shows only a slight difference in the LSPR wavelength, as shown in Figure 2.4 and slight sharpening of the LSPR peaks for smaller NA. It was caused by the smaller angle of incident light, which results in excitation of horizontal plasmonic modes rather than vertical ones. The vertical modes lower the signal and broaden the LSPR [45]. Therefore, the following transmittance measurements were done with the closed aperture stop and 10×, 0.25 NA objective.

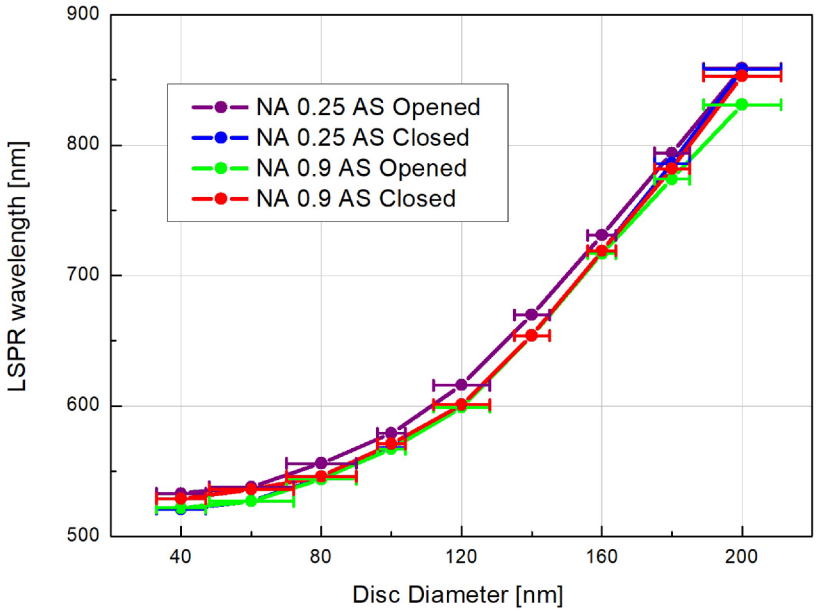

Figure 2.4: LSPR wavelength, extracted from the extinction spectra, as a function of the nanodisc diameter. Nanodiscs are aligned in the square 100×100 μm array with the 3d pitch. This graph compares 2 different collecting objectives (NA 0.25 and 0.9), each of them in combination with either opened or closed AS.

Dark-field (DF) microscopy is a great instrument for measuring the LSPR of a single NP [57–59]. As shown in Figure 2.5, the light, in DF mode, illuminates the substrate and NP under the specific angle. The incident light is reflected from the smooth substrate almost under the same angle and cannot arrive into the central part of the objective. Therefore, the smooth substrate seems dark. The NP, on the other hand, scatters the light due to the LSPR. As there is always part of the spectrum that illuminates the objective, due to surface and instrument imperfections, we had to divide the measured signal with the Broadband Hybrid Diffuser from the company Edmund optics, as a reference.

Single GNDs were fabricated 10 μm apart. After measuring the signal in the DF with 100×, 0.9 NA objective and dividing it with the aforementioned reference, we acquired data for nanodisc diameters from 60 nm to 200 nm (see Figure 2.6a). The results were compared with the FDTD simulation, which was carried out for the single GND with the adhesion layer illuminated by the perpendicular (to the surface) planar wave.

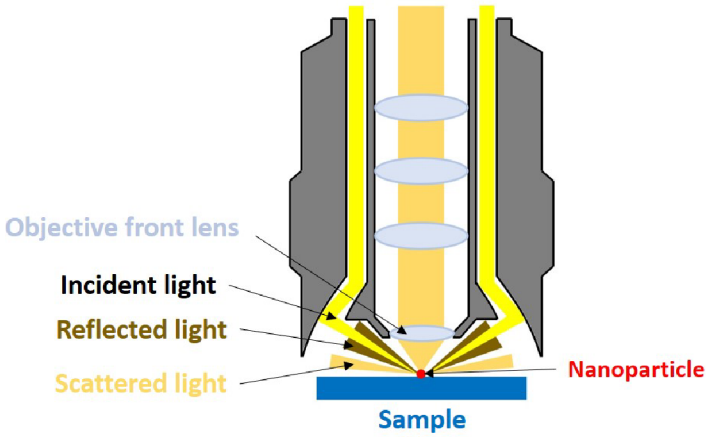

Figure 2.5: Schematic principle of dark field microscopy. Incident light illuminates a sample and a NP on top of it under a large incident angle. The substrate reflects the light under the same angle, thus avoiding the objective lens, and consequently seems dark. The NP, on the other, scatters the light and appears in the image as a bright object, which would be normally invisible in a BF mode.

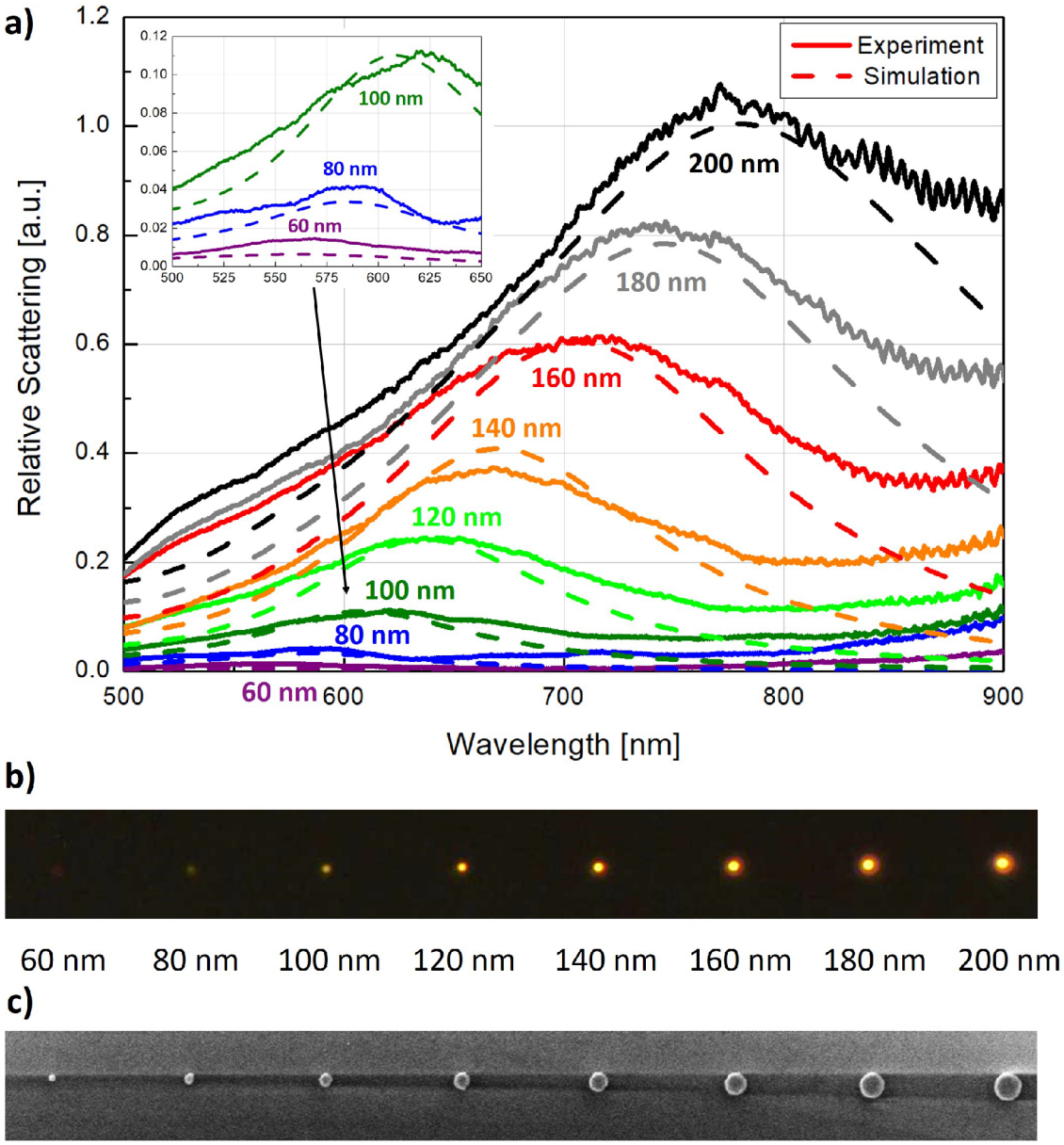

Figure 2.6: a) Relative scattering, as the function of wavelength, for various 50 nm high single GNDs with 3 nm Ti adhesion layer. It compares experimental data with the numerical simulation. b) DF image of the measured single GNDs. c) SEM micrograph of the measured single GNDs.

Despite using the incident light perpendicular to the surface in the simulation and the light under the angle in the experiment, we can see a rather good agreement of the simulated data with the experiment. The extinction variation of the smaller diameter nanodiscs can be caused by the fabrication imperfections. Based on these results, we can conclude that the LSPR of single nanodiscs can be precisely measured with DF microscopy. On top of it, results of this DF measurement are comparable with the simulation of single nanodiscs, illuminated by the perpendicular planar wave. This simulation is one of the easiest and least time consuming simulation to be carried out.

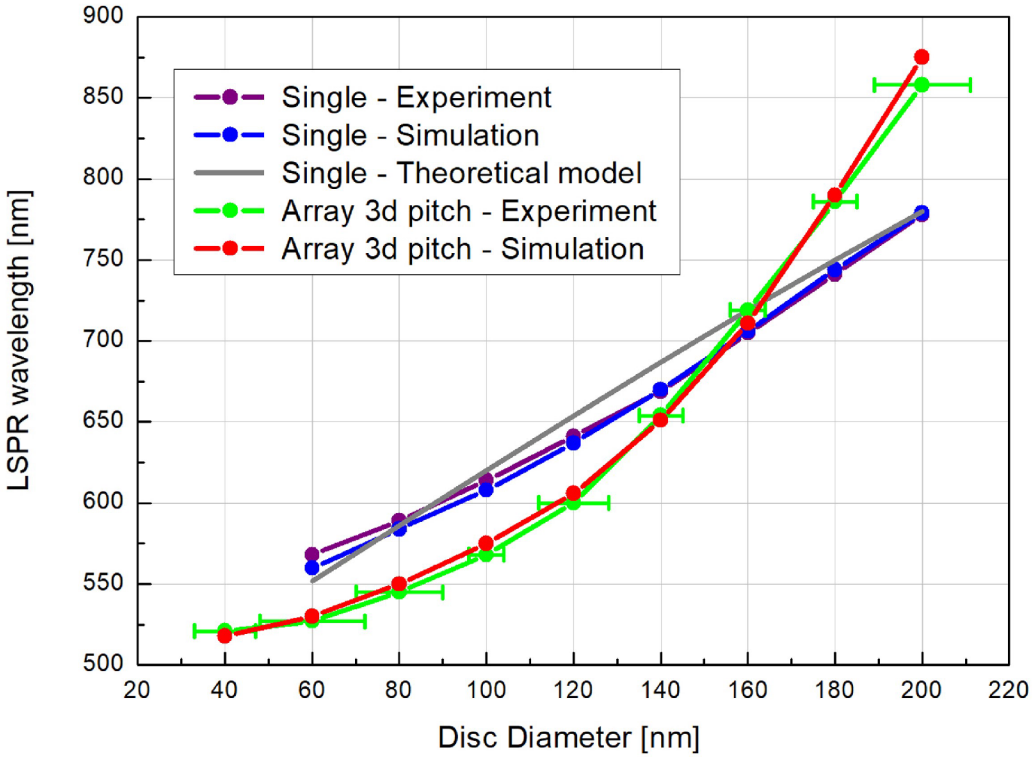

Figure 2.7: LSPR wavelength, as the function of nanodisc diameters, extracted from the extinction spectra. We compare the single GNDs measurement, theoretical model and simulation with GND arrays measurement and simulation. In the case of arrays, nanodiscs diameters involve error bars, representing non conformal diameters.

We now take a closer look at the LSPR wavelength as the function of disc diameters, comparing the single GNDs and GND arrays measurement, simulation and theory. In Figure 2.7 we can observe a good match between the simulated and experimental data for both cases. The experimental and theoretical results, on the other hand, shows slightly different behaviour. While the experimental and simulated LSPR wavelengths follow really wide exponential dependence, the theoretical model follows the square root function dependence. This difference is caused by the approximation made for the theoretical model, where the height of the nanodisc is much smaller than the diameter. If we carry out the simulation for 40–200 nm diameter GNDs with the height varying from 1–100 nm (see Figure 2.8a), we find out that, coming down to the 1 nm height, the approximation can take place and the LSPR wavelength function of GNDs follow the theoretical dependence. Another interesting event occurs, when the height increases. The square root function dependence changes through the linear dependence (for the 10 nm height) into the exponential dependence. By carrying out the LSPR wavelength as the function of the height for various GND diameters (see Figure 2.8b), we find out the indirect square root proportionality to the height, supporting the theoretical model even more. Therefore, we can say that the theoretical model is correct, when the above-mentioned approximation is fulfilled. The LSPR wavelengths of GNDs with tens of nanometers in the diameter exhibit an interesting behaviour, which will not be developed in this thesis any further, but its nature could be developed in the future work, as it was not, to our knowledge, examined in any research, yet.

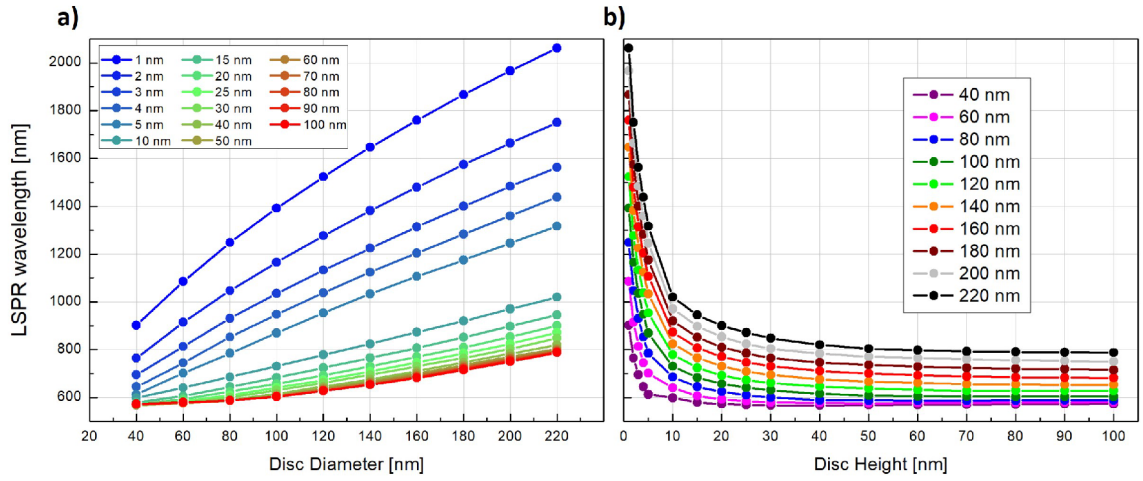

Figure 2.8: a) Simulated LSPR wavelength of the single GNDs, as the function of the disc diameter. b) Simulated LSPR wavelength of the single GNDs, as the function of the disc height.

Another fact, in Figure 2.7, worth noting, is the difference between the LSPR wavelength of single GNDs and GND arrays. The difference is caused by dipole-dipole interaction, as resonating nanodiscs act as dipoles and interact with each other [52, 60]. The interaction results in alternation of the polarizability α in Eq. (2.6) by the retarded dipole sum [53]

$$\alpha \to \frac{\alpha}{1-\alpha S}\,, \quad S = \sum_{j\neq i}\left(\frac{(1-ikr_{ij})\,(3\cos^2\theta_{ij}-1)\,e^{ikr_{ij}}}{r_{ij}^3} + \frac{k^2\sin^2\theta_{ij}e^{ikr_{ij}}}{r_{ij}}\right). \tag{2.12}$$

This sum depends on the distance between the particles r_{ij} and on θ_{ij}, the angle between the polarization vector and vector from nanoparticle i to j. The first element in the sum can be referred to the near-field interaction of discs, which is significant when the nanodiscs are up to 30 nm apart [61–63]. When nanodiscs get further apart, the second (far-field) element in the sum takes over [52, 60]. As our GND arrays has 3d pitch, with the 120 nm pitch for the smallest diameter of the nanodiscs, we consider only the far-field interaction.

The far-field interaction is what we wanted to understand better, as VO_2 and FeRh experiments were done within the array. Thus, we carried out the simulation of 50 nm high GND arrays for the above-mentioned diameters with various pitches. In Figure 2.9a we can see that LSPR wavelengths increase, until they hit the specific distance, and drops. Due to this drop we carried out also the simulation for the 50 nm high GND arrays with the 140 nm diameter, where the step of the pitch was 20 nm (Figure 2.9b). In this second graph we can observe the red-shift of LSPR wavelength with the increasing pitch distance, which stops at 500 nm pitch — called the critical pitch or critical grid spacing [64]. The nature of this behaviour is referred to a diffraction order (DO), which is responsible for the dipole-dipole interaction when a grating order changes from evanescent to radiative [65, 66]. Resonance wavelengths then follows another

relation, expressed generally as [67]

$$\lambda_{\mathrm{DO}} = \frac{2\pi n_{\mathrm{substrate}}}{\sqrt{\left(k_x + N_x \frac{2\pi}{P_x}\right)^2 + \left(k_y + N_y \frac{2\pi}{P_y}\right)^2}}, \tag{2.13}$$

where k_x and k_y are the k-vector components of the incident light, N_x and N_y the diffraction orders in the xy basis, P_x and P_y the pitch in the xy basis, and $n_{\mathrm{substrate}}$ is the refractive index of a substrate. In our simulation, we had the normal incidence ($k_x = k_y = 0$). Incorporating the diffraction orders (1,0) or (0,1) into the equation, we came up with the function shown in Figure 2.9b. The variation between the model and simulation, up to the 500 nm pitch, is consistent with the previous observations by Schatz and co-workers [53]. Above the 500 nm pitch we observe a decrease that stops at the constant value. It probably happens because the DO resonances diverge from the simulated spectrum, leaving the LSPRs behind. We assume these LSPRs are still influenced by DO resonances, as the LSPR wavelength of the array does not match the single nanodisc LSPR wavelength.

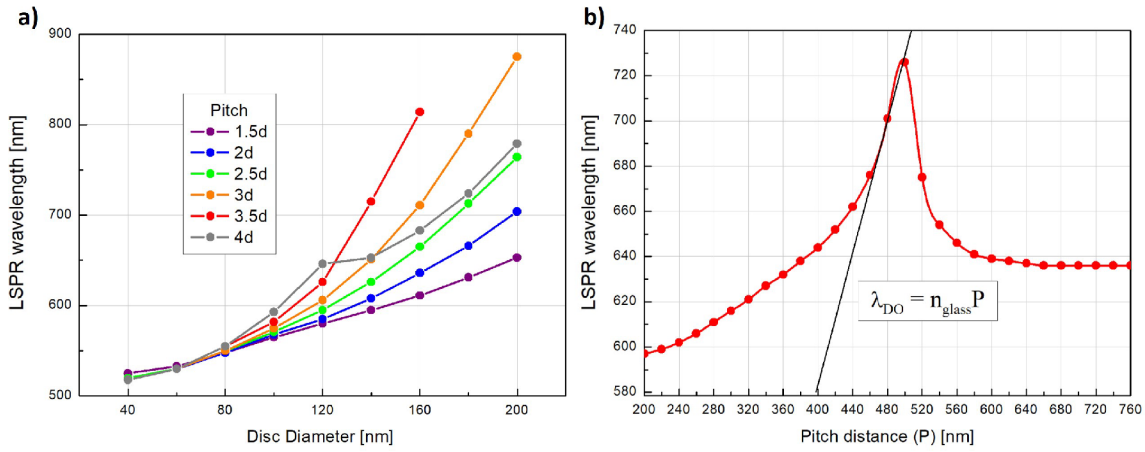

Figure 2.9: a) Simulated LSPR wavelength of the 50 nm high GND arrays, as the function of their nanodisc diameters for various pitches. b) LSPR wavelength as the function of the pitch distance. The red line refers to simulated data of the 50 nm high GND arrays with the 140 nm disc diameter. The black line represents the theoretical model of DO resonances for the normal incidence and diffraction orders (1,0) or (0,1).

So far, we measured GND arrays in the BF mode and the single GNDs in the DF mode. As the single nanodisc measurement were not possible in the BF mode, due to the weak signal of nanodiscs, we measured the GND arrays with the 3d pitch also in the DF mode. Starting with the 100×, 0.9 NA objective, we observed changes in colors of those arrays (the left side of Figure 2.10) as expected from the LSPR wavelengths. Due to our curiosity, we changed the objective and suddenly observed a completely different array coloring for the each of objectives listed in Figure 2.10. Assuming, it had something to do with the pitch in the array, we produced new GND arrays with the same diameters, but fixed 480 nm pitch. Our assumption was partially confirmed, when we examined new arrays (the right side of Figure 2.10). The coloring of new arrays for the 10×, 20× and 50× objectives stayed almost the same. For the 100×, 0.9 NA objective colors of arrays did not change significantly compare to observation

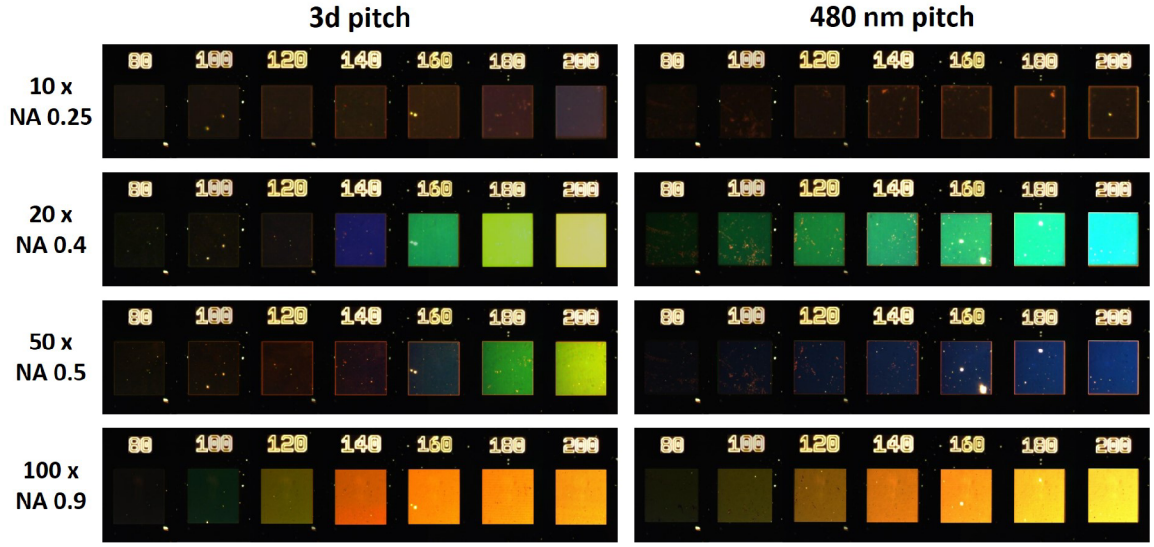

Figure 2.10: DF images of the gold nanodisc arrays with the diameter of the individual nanodiscs inscribed above each array. The images were taken using four objectives, listed on the left side of the image. The arrays on the left side have varying 3d pitch, while arrays on the right side have fixed 480 nm pitch.

of the first sample with the same objective. Looking at the relative scattering from the measurements with 10×, 20× and 50× objectives, the distinctive colors were so strong that we were not able to measure the LSPR wavelengths any more. For the measurement with the 100×, 0.9 NA objective, the situation was different. Both types of arrays (with 3d and 480 nm pitch) showed resonances that referred to the LSP and pitch (Figure 2.11). It is nicely visible how varying pitch resonances, for the 3d pitch arrays, travel together with the LSPRs (Figure 2.11a), while fixed pitch resonances stayed on the spot, for the 480 nm pitch arrays. On this two graphs, we assume that we observe both shifted LSPRs and diffraction order resonances, referred to the pitch.

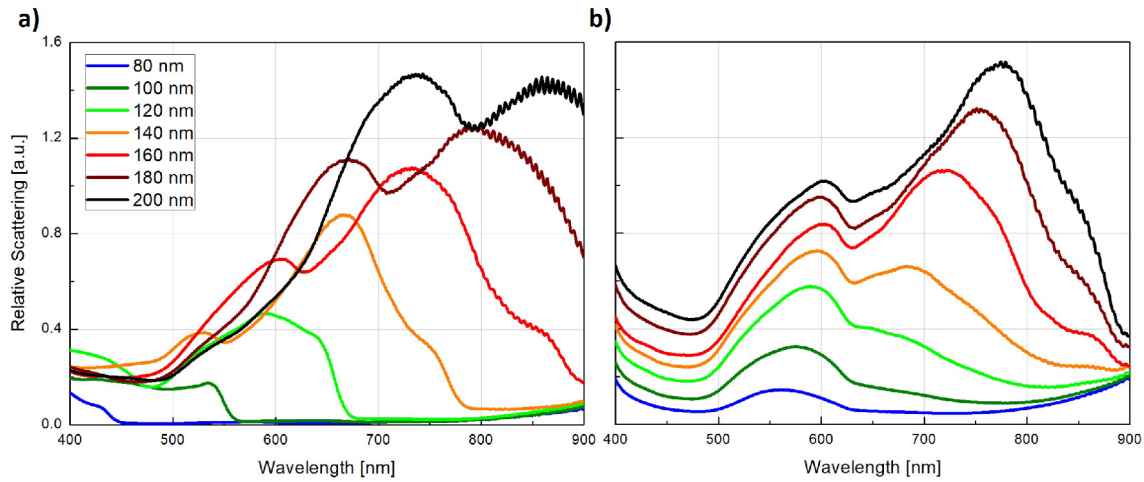

Figure 2.11: The relative scattering cross-section of GND arrays with the a) 3d pitch and b) 480 nm pitch measured with the 100×, 0.9 NA objective in the DF mode.

The color of arrays seemed to be dependent not only on the pitch, but also on the objective. As objectives generally illuminate the sample under the same angle, what differs them is the angle of collection. In any case, the angle played the second key role in this observation, right after the pitch. Therefore, looking at Eq. (2.13) we got ensured, we were dealing with the above-mentioned diffraction order. As the k_x and k_y were not equal to zero, the whole behaviour was more complex and therefore needed deeper investigation.

This chapter began by describing plasmonics and its applications, with a particular emphasis on the theory of LSPs and the theoretical model of the LSPR wavelength. This model did not match the experimental a simulation data, as the approximation condition for the height being much smaller than the diameter of the GND was not fulfilled. Deeper examination proved the correctness of the model. After the single GNDs examination, we compared the BF transmittance measurement and simulation of the GND arrays, with the DF measurement and simulation of the single GNDs. The comparison of the LSPR wavelengths proved the concept of the far-field (dipole-dipole) interaction in arrays. This interaction was the result of diffraction order, which was examined on the simulated data of varying pitch for the fixed diameter GND. Also DF measurements of GND arrays proved the concept of diffraction order, but with more complex behaviour, as the angle of incidence and collection were specific for various objectives. Overall, this chapter gave us better understanding of the theory of plasmonics and BF transmittance and DF reflectance measurement.

3. Phase-change materials

When talking about phase-change materials (PCMs), the first material that usually comes to one's mind is water. By applying external energy in a form of heat or pressure, the ordered molecules of the solid water break down to less ordered molecules in the liquid. The most common PCMs transform from the solid to the liquid phase by melting at the specific temperature. It mostly results in modification of their electrical and optical properties [68]. Beside the solid–liquid transition, there are others, out of which the solid–solid transition receives higher attention in nanotechnology research than other transitions. This type of the transition is associated with a crystalline change from one lattice configuration to another. It results in modification of their electrical [69], optical [47] or magnetic [70] properties, which have numerous applications [71–73].

In this work, we focus on vanadium dioxide (VO_2), due to its modification of electrical properties, and iron-rhodium alloy (FeRh), due to the modification of magnetic properties. After introducing the detailed mechanism of their transition and current applications in plasmonics, we will continue with optimization of growth of polycrystalline VO_2, and subsequently will measure the optical response of nanodiscs made of these materials.

3.1 Vanadium dioxide

One of the most promising solid–solid PCM is VO_2. It exhibits a metal–insulator transition (MIT) at approximately 67 °C for bulk crystals [74]. Having the MIT temperature closer to the room temperature than other oxides, the VO_2 transition does not require that much energy. Beside heat, the energy needed for the MIT can be applied in a form of electrical, magnetic, optical or strain stimuli [75].

The VO_2 advantage lies not only in the low MIT temperature, but also in the significant change of its electrical and subsequently optical properties. For example, a change of resistivity around four orders of magnitude was observed during the transition from its insulator form into the metallic one [76]. The responsible factor is a reconfiguration from the monoclinic crystal structure into the metallic rutile structure [77]. We can notice the transformation of atomic distances, which causes cancellation of the band gap in the insulator phase and increases amount of electrons in the conduction band (see Figure 3.1). Looking closer at the nature of this transition, there are two possible explanations for the above-mentioned reconfiguration. The first is based on the Mott–Hubbard theory, where strong correlation between electrons leads to their localization and subsequently creation of the band gap [78]. The second explanation is based on the Peierls theory, where an oscillation of atomic cores causes creation of ion dimers, which split the dispersion relation and opens the gap at Fermi-surface [79].

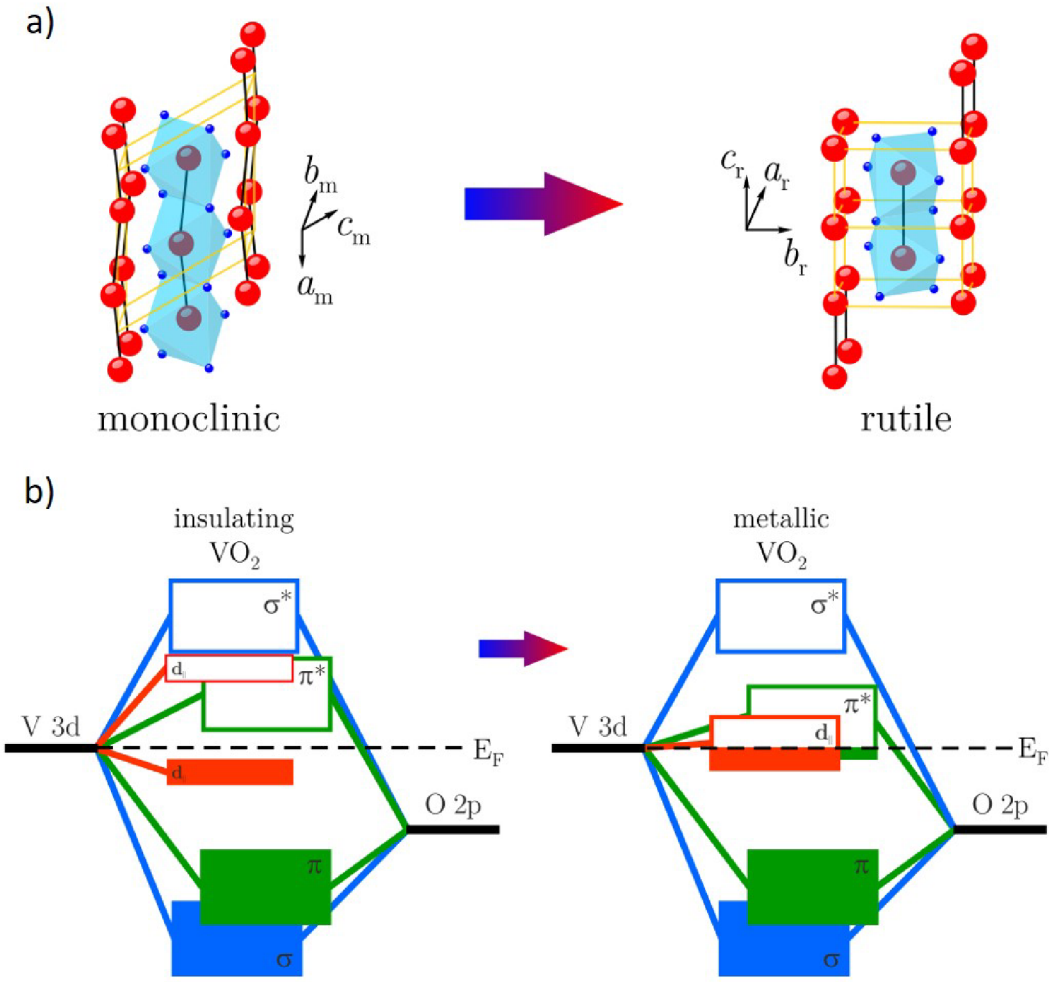

Figure 3.1: a) VO_2 transition from the insulator monoclinic structure to metallic rutile structure. b) Scheme of VO_2 band structure in its insulator form and in its metallic form. It shows cancellation of the band gap ($\approx 0.7\,\mathrm{eV}$) and cross-linking the conduction and valence band. Adapted from [47].

Whether the correlation effect of electrons or the structural change are driving forces of the MIT has been the subject of much debate [78]. The MIT naturally influences the dielectric function, as shown in Figure 3.2. We can see a strong drop of the real part in the near-infrared (NIR) spectrum, when VO_2 is heated above the MIT temperature. This drop is also interesting for plasmonics, as the real part of the dielectric function for the metallic phase pass negative values, opening the possibility for the LSPR [79].

Dealing with the bulk and thin layers of VO_2, the increase of electrons in the conduction band has many applications. The resistive switching [80], solar cells and smart window coatings [81], sensors [82], variable-reflectivity mirrors [83],and many others [84] are well known for a couple of years. On the other hand, incorporating a thin layer of VO_2 as a substrate under plasmonic nanostructures [85], or directly structuring this tunable material into the metasurface [86] are examples of less explored applications and, therefore, a subject of many ongoing experiments. On top of those applications, VO_2 thin layers and nanostructures exhibit ultra-fast MIT switching [87], which can result in more promising applications of fast-tunable metasurfaces.

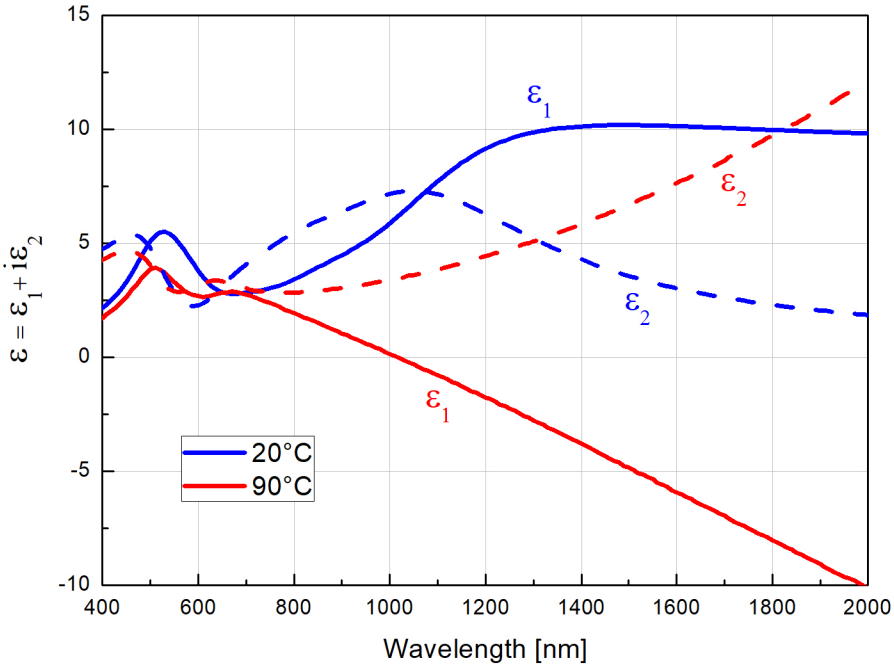

Figure 3.2: Real and imaginary of the dielectric function of VO_2 at 20 °C and 90 °C and, therefore, of the insulator and metal phase, respectively. Adapted from [47].

To deposit thin layers, or fabricate VO_2 nanostructures, various methods can be incorporated. The deposition can be done with magnetron sputtering [88], electron beam evaporation [89], or pulsed laser deposition (PLD) [90] from vanadium or vanadium dioxide targets. As we are dealing with an oxide, the annealing in oxygen atmosphere during [91] or after the deposition [92] needs be executed. To choose the best method and process parameters, it is common to compare hysteresis contrasts and widths of VO_2 resistivity or transmittance during the MIT. In the next section, we will describe the optimization of the polycrystalline growth of VO_2 thin layer by the electron beam evaporator. Afterward, we will create plasmonic nanodiscs of out the optimized VO_2 and measure their optical response.

3.1.1 VO_2 growth optimization

The various methods mentioned in the previous section can be employed for the growth of bulk polycrystalline VO_2. We decided to work with an electron beam evaporator from the Bestec company due to user-friendly software and possibility to deposit VO_2 even onto whole 4-inch wafer. The electron beam acts as a source of focused energy, that heats the VO_2 powder stored in a molybdenum crucible. As the deposition without annealing process was not enough to create VO_2, the deposition with post-annealing in oxygen atmosphere had to be incorporated. Because the source of electrons is a tungsten filament that could burn out in oxygen atmosphere, the post-annealing in oxygen atmosphere was not possible in the evaporator. The annealing process of the thin layer, deposited in the evaporator, was thus performed in a PLD chamber, where the temperature and partial pressure of various gases can be precisely controlled.

The optimization was done on seven samples, which were firstly coated with 50 nm thin layer of a vanadium oxide with an unknown stoichiometry, as it did not exhibit MIT. After the deposition, they were annealed in oxygen atmosphere for the fixed 0.333 mbar pressure (following [88, 92]) and various annealing temperatures and times (see Figure 3.3). The grey regions on the samples are places, where the unknown stoichiometry was kept even after the annealing process. The yellow regions represent another stoichiometry, created from the grey one, when the annealing temperature was high enough. For two samples, only parts under the metal holder changed color, from the grey to the yellow, as the direct contact of the VO_2 layer with the metal part resulted in an uncontrolled higher temperature. Too high temperature seems to even burnt down the thin layer of VO_2.

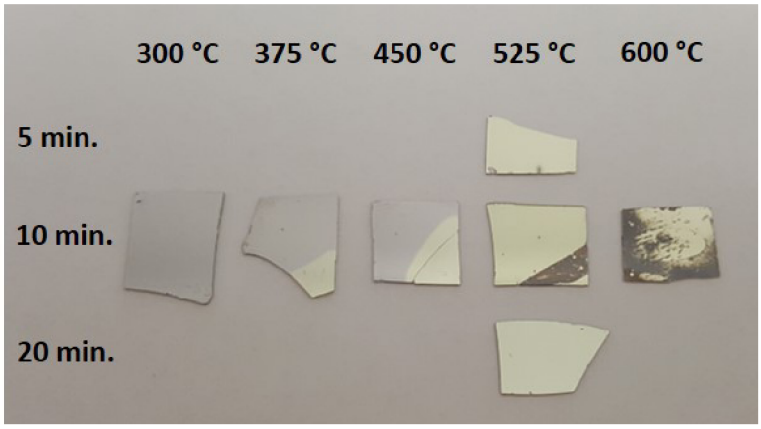

Figure 3.3: Photograph of seven SiO_2 samples covered with a 50 nm thick layer of VO_2 on the electron beam evaporator. They are ordered in a matrix, where the columns represent different annealing temperatures and the rows different annealing times.

To characterize the thin layers and compare their quality, we measured their transmittance in the visible part of the spectrum for temperatures from 30 °C to 90 °C with 5 °C steps. The reference was taken from the same place at 30 °C. The grey regions showed no MIT, while the yellow regions, created after the annealing, exhibited a change of transmittance around 70 °C. Thus, we confirmed creation of VO_2 after the annealing process. The highest increase of transmittance was observed at around 700 nm wavelength, as shown in Figure 3.4a. Based on the transmittance contrast between 30 °C and 90 °C at 700 nm wavelength (Figure 3.4b,c), we found out that the sample annealed

in the oxygen atmosphere at 525 °C for 10 min exhibits the biggest optical change for the 50 nm thin layer of VO_2. Measuring the optimized sample with an AFM revealed only slight grouping of approximately 10 nm surface grains before the annealing into the 20 nm surface grains after the annealing (Figure 3.4e). This grouping should not influence production of VO_2 nanodiscs.

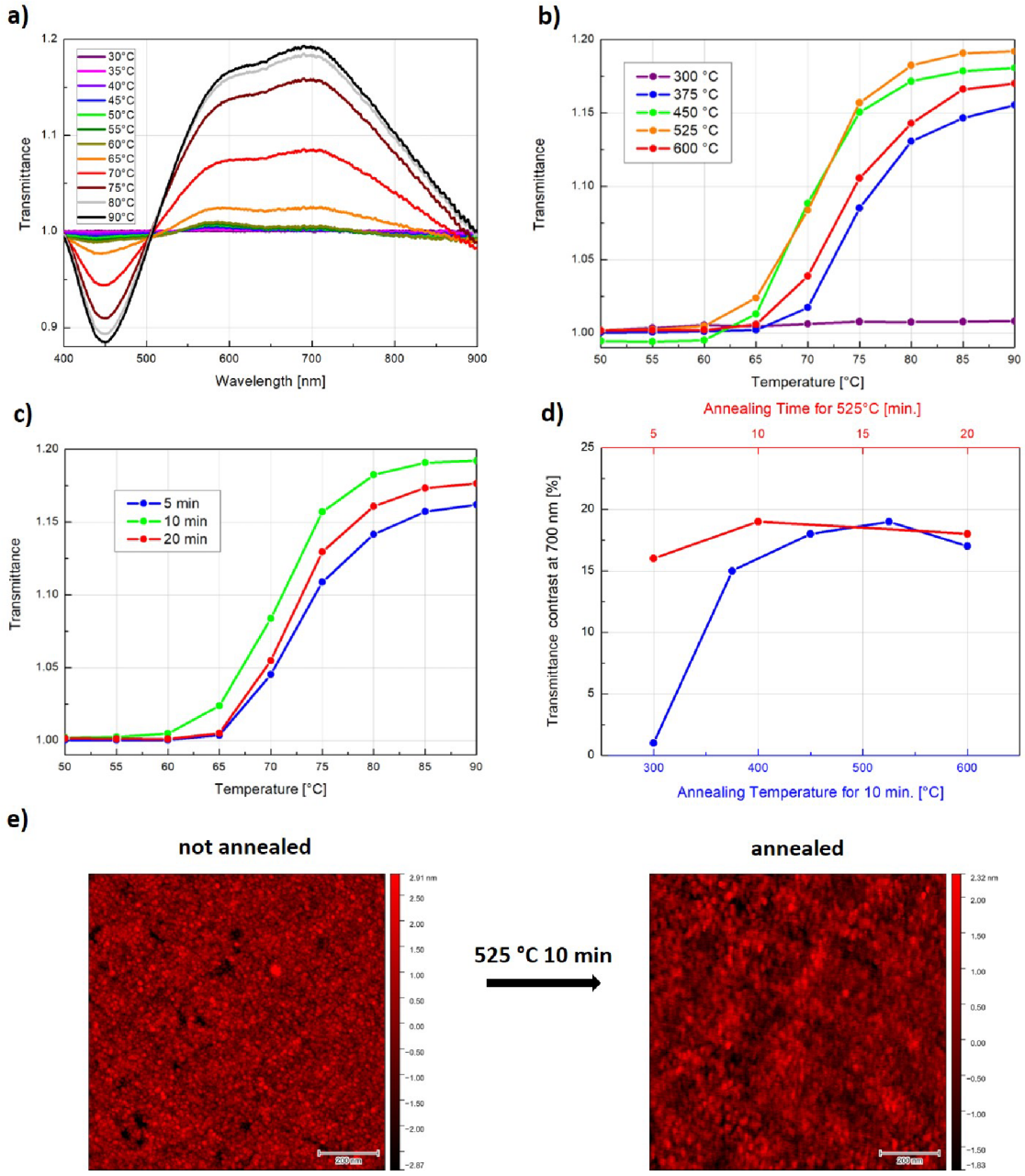

Figure 3.4: a) Transmission spectra for a 50 nm layer of VO_2 on SiO_2. The transmitted signal at 30 °C is taken as a reference. The spectrum is measured in 5 °C steps, where the sample was annealed at 525 °C for 10 min. b) Transmittance at the wavelength of 700 nm for the fixed annealing time of 10 min and varying annealing temperature. c) Transmittance at the wavelength of 700 nm at fixed 525 °C and varying annealing time. d) Relationship between the transmittance contrast and the annealing temperature extracted from the spectra in b) and c). e) AFM image of the sample, annealed at 525 °C for 10 min, before and after the annealing.

3.1.2 VO_2 nanodiscs measurement

After we optimized the polycrystalline VO_2 growth using the metric of the transmittance contrast, we moved to the fabrication of nanodisc arrays. Again, we applied the optimized EBL process, where arrays of 50 nm high nanodiscs of 80–300 nm in diameter were fabricated onto the SiO_2 substrate. The array pitch was set to three-times the nanodisc diameter. The nanodiscs were produced before the annealing process, as the positive resist would not withstand the high annealing temperature. An interesting behavior occurred during the lift-off process. First, an ultrasound treatment, normally used during the gold nanodiscs lift-off, always destroyed the nanostructures. We assume, the reason was poor adhesion of the VO_2 nanodiscs. Applying titanium as adhesive layer under VO_2 did not help. Therefore, the ultrasound should not be used for VO_2 nanostructures at all. Second, the liquid remover also destroy VO_2 nanostructures, when the sample was kept in it over night. If the sample was kept in the remover one hour, the remover did not erase nanostructures, but caused the decrease of approximately 20 nm in nanodisc diameters. Shortening the lift-off process time did not provide full removal of the residual resist. Thus, the lift-off of the VO_2 nanostructures need to be carried out in approximately one hour without the ultrasound treatment.

Another interesting behavior occurred after the annealing process. When we measured the transmittance contrast on a $200\times200\,\mu$m VO_2 square, fabricated next to the arrays, we found out that it does not exhibit the same transmittance contrast as the previously optimized large-scale thin layer (see Figure 3.5a). So, we measured the optical response of the arrays at 30 °C and 90 °C and annealed the whole sample once again, at 600 °C for 10 min. The annealing at higher temperature resulted in an enhanced transmittance contrast (see Figure 3.5a), which also effected the optical response of nanodisc arrays (compare Figure 3.5c with Figure 3.5d). We propose three possible causes: the annealing temperature and time depend on the size of the particle, the deposition and annealing procedures are too sensitive and therefore hardly reproducible, or the transmittance contrast is not an appropriate metric for the quality measurement. The deeper research needs to be carried out in this matter.

Nanodisc arrays were measured in the visible part of the spectrum at 30 °C and 90 °C. The measurement was done after the first (Figure 3.5c) and also after the second (Figure 3.5d) annealing process. In both dielectric phases, we measured resonances for nanodisc arrays with diameter bigger than 177 nm. These resonances were more pronounced and also slightly red-shifted after the second annealing, where the transmittance contrast improved. The observed resonances can be referred to as Mie's dielectric resonances [93]. They received a growing interest in the recent years, due to minimal loses during the resonance [94]. When the sample was heated and VO_2 nanodiscs underwent the MIT, the resonances disappeared. To observe LSPRs of the metallic VO_2 nanodiscs, we would need to move to the NIR spectrum, where the condition for the negative real part of the dielectric function (Figure 3.2), represented by the Eq. (2.6), is fulfilled. Similar LSPRs of metallic VO2 nanodiscs were measured by Appavoo et al. and are reproduced in Figure 3.5b. Combining their results for the high-temperature phase with our results for the low-temperature one, an interesting opportunity for further research arises. That is, if we measure the extinction spectra of the given arrays in NIR, we could be able to observe the change from Mie's dielectric resonances to LSPRs.

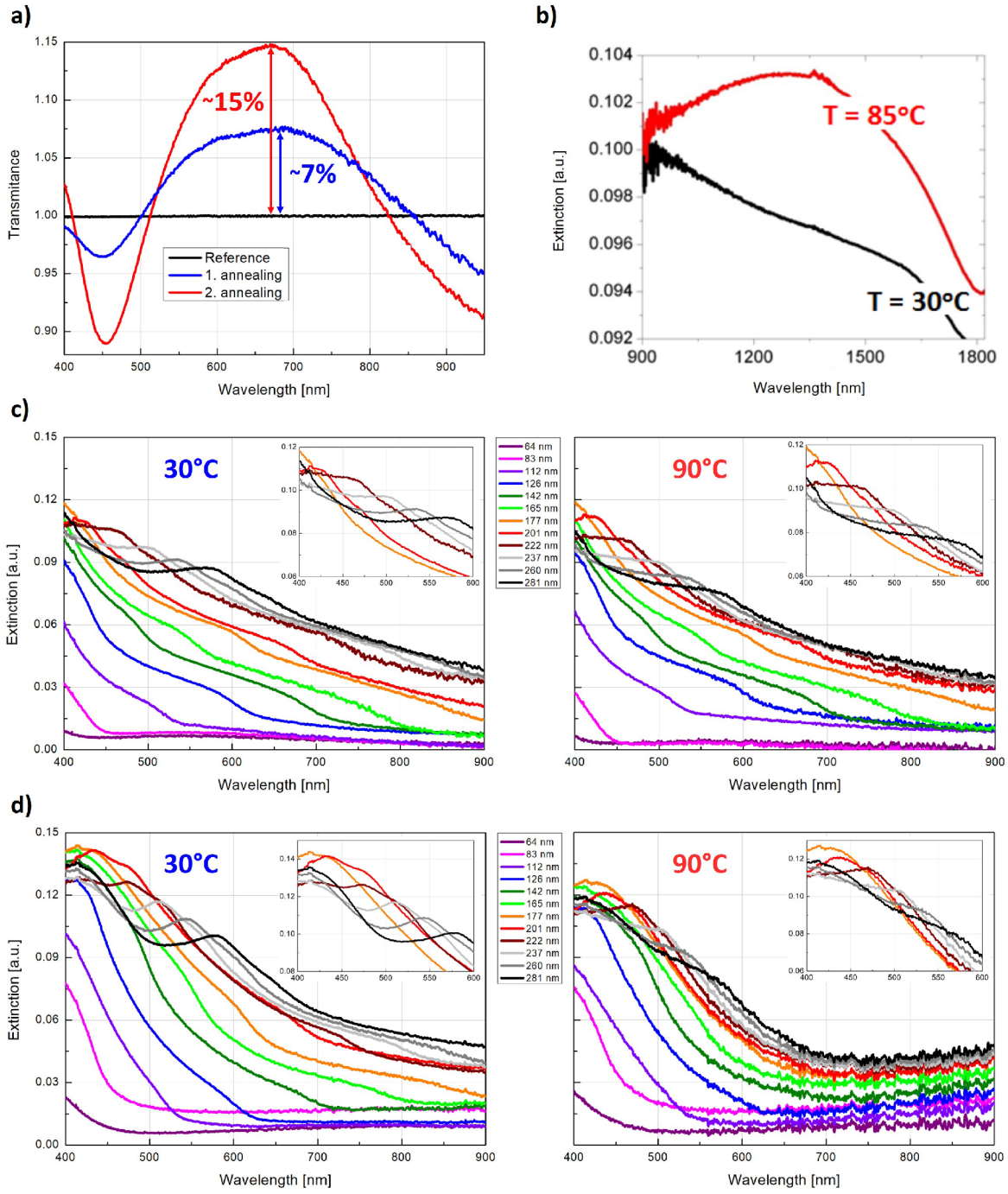

Figure 3.5: a) Transmittance contrast of 200×200 μm VO_2 square. The first annealing process at 525 °C for 10 min is compared with the second annealing process at 600 °C for 10 min of the same sample. b) Extinction spectra of a single VO_2 nanodisc with 210 nm diameter during its MIT. Adapted from [79]. c) Extinction spectra of VO_2 nanodisc arrays after the first annealing process. d) Extinction spectra of VO_2 nanodisc arrays after the second annealing process. Measurements of c) and d) were taken in dielectric (at 30 °C) and metallic (at 90 °C) phase of VO_2.

3.2 Iron-rhodium alloy

Apart from VO_2 we investigated also another solid–solid PCM — FeRh. Instead of the MIT, FeRh undergoes a phase transition from an antiferromagnetic (AF) to a ferromagnetic (FM) phase at approximately 87 °C for bulk alloys [95]. During this transition, a collinear spin structure of the AF phase, with the magnetic moment of 3.1 μ_B per Fe and no magnetic moment per Rh, changes into the FM phase, with the moments of 3.2 μ_B per Fe and 1.0 μ_B per Rh [70] (as depicted in Figure 3.6a). Beside the change in the magnetization, FeRh exhibits also a slight alternation of its resistivity [96]. The resistivity and magnetization changes enable new approaches in magnetic refrigeration [97] and recording [98], new metallic memory cells [99], and others [100].

To find out possibility of LSPRs, we had to measure the dielectric function of FeRh. The dielectric function was taken by an ellipsometry measurement of the 20 nm thick FeRh layer (Figure 3.6b). As the MIT temperature varies based on the quality of FeRh layer, the MIT temperature for our measured layer was at 87 °C. Because the change in its resistivity is not substantial, as it was for VO_2, we do not observe any significant change in its dielectric function during the AF-FM transition. In any case, the idea behind the FeRh nanostructures was not to create another tunable metamaterial, but to observe LSPRs of FeRh nanostructures in the visible part of the spectrum. We can see that its real part acquires negative values in the visible part of the spectrum, fulfilling the LSPR condition. This way, we should be able to observe LSPRs of FeRh nanostructures, when illuminating by visible light.

To receive the above-mentioned AF-FM transition of FeRh, FeRh needs to have the specific bcc structure. This structure needs to be grown epitaxially on a magnesium oxide (MgO) or sapphire (Al_2O_3). Due to the epitaxial growth the deposition is a delicate process. FeRh is mostly produced by magnetron sputtering from an FeRh target [96]. We used this very same method for a fabrication of a set of FeRh nanodisc arrays and we examined their plasmonic properties.

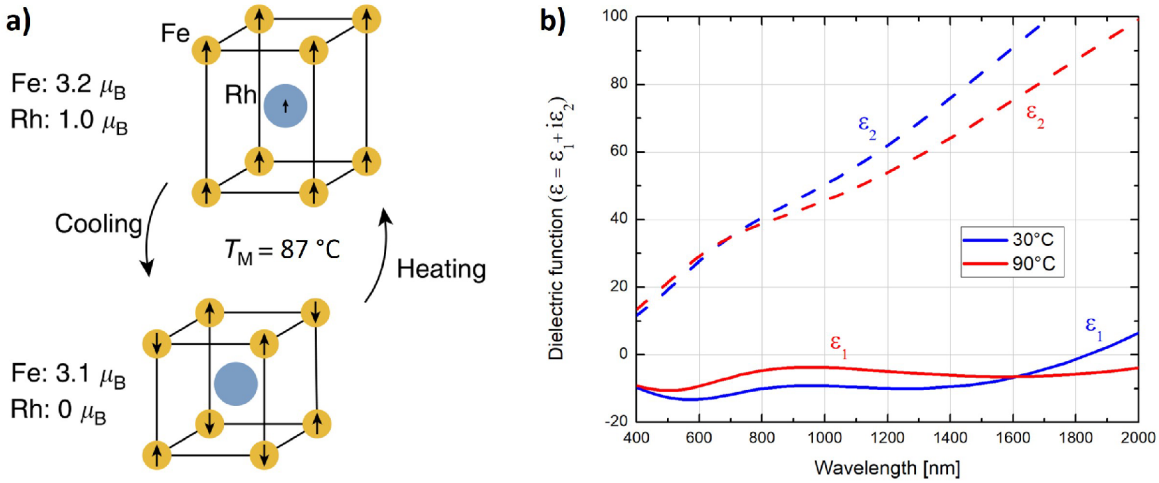

Figure 3.6: a) Illustration of FeRh crystal structure before and after the transition from the AF phase into the FM phase and vice versa. Adapted from [96]. b) Real and imaginary part of FeRh dielectric function before and after the transition. Adapted from an unpublished ellipsometry measurement by F. Ligmajer.

3.2.1 FeRh nanodiscs measurement

As FeRh needs to be grown epitaxially and an annealing step is required during the deposition, our optimized EBL process, which uses a positive resist that would burn down, had to be adapted. A deposition of a 20 nm thick FeRh layer on top of a MgO substrate by magnetron sputtering was done by Jon Ander Arregi. Parameters of the deposition can be found in [96]. The magnetization measurement of this layer showed that the transition temperature, for this thin layer, is about 120 °C (Figure 3.7a). After that, Jan Hajduček fabricated FeRh nanodiscs, following a different EBL procedure compared to the one used for fabrication of Au and VO2 nanodiscs. First, he deposited a 64 nm layer of SiO_2 using an electron beam evaporator and 120 nm of a negative resist (AR-N 7520.07) from the Allresist company on top of the FeRh layer. The nanodiscs fabricated that way served as a shadow mask for the subsequent etching of SiO_2 in hydrofluoric acid, followed by reactive-ion etching (RIE) of FeRh with argon ions. After stripping the residual resist in a liquid remover and SiO_2 in hydrofluoric acid, we obtained FeRh nanodiscs, whose diameters increased, compared to planned, during the procedure. Out of the planned nanodisc arrays with 3d pitch and diameters 60–180 nm, we ended up with the same array confinement, but all diameters were about 80 to 90 nm bigger that the expected values (see Figure 3.7c).

The fabricated nanodisc arrays were measured by BF transmittance mode in the visible part of the spectrum, in the same way as Au and VO_2 arrays, and their extinction spectra can be seen in Figure 3.7c. To have the clearer image of the LSPRs, we carried out also the normalized extinction spectra in Figure 3.7d. As the heating stage did not allow us to reach the transition temperature (120 °C) for the thin layer, we measured the extinction of FeRh discs for 30 °C and 90 °C. Already for these temperatures, we noticed slight changes in LSPR wavelengths (Figure 3.7b), which could be even more interesting to examine for the temperature above the MIT.

In this chapter we focused on solid–solid PCMs, specifically VO_2 and FeRh. We described the detailed mechanism of their transition and current applications. After optimizing the evaporator/annealing procedure of the polycrystalline growth of VO_2, we fabricated VO_2 nanodiscs onto the SiO_2 substrate and measured their optical response. We observed Mie's resonances in the VO_2 dielectric phase, which in combination with the metallic plasmonic resonances in the NIR spectrum could be an interesting fact to be examined. After the alternated fabrication of FeRh nanodiscs, we measured their optical response. Even we did not observed the significant change during the AF-FM transition, observing the LSPRs in the first place already fulfilled our goal.LSPRs of FeRh nanodiscs could be subsequently used for the enhancement of the FeRh transition.

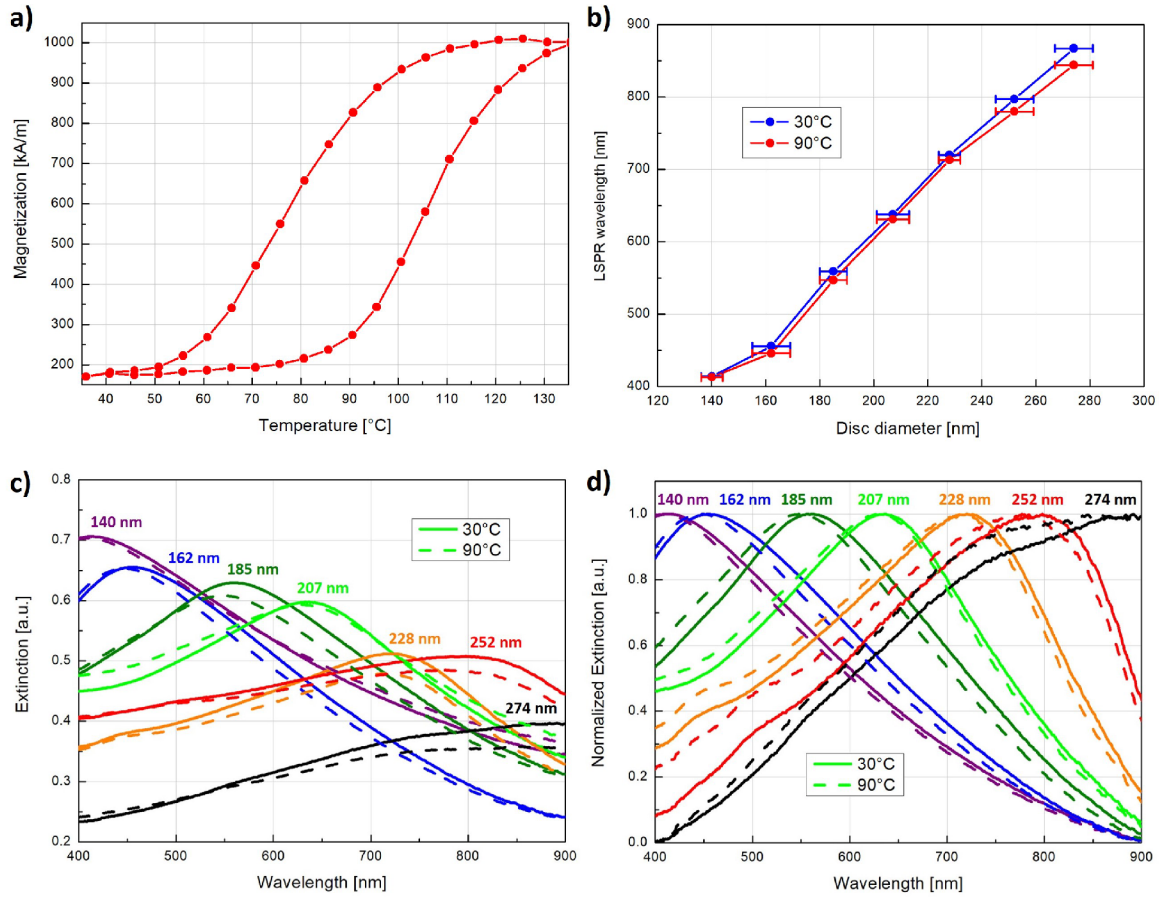

Figure 3.7: a) Magnetization of the 20 nm high FeRh thin layer as a function of temperature. Adapted from an unpublished magnetization measurement by J. A. Arregi. b) LSPR wavelengths of FeRh nanodiscs at 30 °C and 90 °C. c) Extinction and d) normalized extinction of FeRh nanodisc arrays of various diameters at 30 °C and 90 °C.

Conclusion

This thesis was focused on the localized surface plasmon resonances in the phase-changing nanostructures. It began with an introduction into nanofabrication, where we compared the most popular nanofabrication methods used nowadays. Based on the precision, time consumption and costs of these methods, we explained our choice to use the EBL for production of our samples. As our thesis was focused on LSPRs of symmetrical nanostructures, we had to optimize the EBL for nanodiscs production. Testing a combination of two resists, two currents, two patterning modes and six doses, we came up with a detailed EBL recipe for the lithographic apparatus in CEITEC Nano laboratories. Following these guidelines, we were able to create gold nanodiscs with sizes down to 40 nm in diameter.

We also introduced the theory of plasmonics, focusing especially on localized surface plasmons. We finished the theory with an equation for the LSPR wavelength as the function of diameter and height of the nanodisc. After introducing the theory, we observed LSPRs for 50 nm high single GNDs and GND arrays with 40–200 nm diameters. The LSPRs, obtained in the BF transmittance measurement of nanodisc arrays, showed a good match with the simulated data. The same match of the measurement and simulated data was observed for the DF reflectance measurement of single GNDs. Even though, the LSPR wavelengths from single GNDs measurement and the above-mentioned theoretical model did not match, due to approximation made in the calculation, further simulations verified the model. Comparing LSPR wavelengths from single GNDs measurement with the GND arrays measurement showed a difference, which was explained as a result of a far-field dipole-dipole interaction within the nanodisc array. Looking closer at the nature of these interactions we observed that resonances, referred to diffraction order, follow different relationship than LSPRs. These findings helped us to better understand the influence of far-field interaction within the arrays on the collective LSPRs.

The last part of this thesis was dedicated to solid–solid PCMs — VO_2 and FeRh. Firstly, we discussed the nature of VO_2 MIT and its applications. Before producing VO_2 nanodiscs, we optimized the polycrystalline VO_2 growth, based on a metric of a transmittance contrast at 700 nm wavelength. Nanodisc arrays made out of the optimized VO_2 films were fabricated onto a SiO_2 substrate and measured in the visible part of the spectrum. The measurement of all arrays was performed at 30 °C and 90 °C. We found out that the VO_2 nanodiscs, in the dielectric phase, exhibited Mie's resonances. We showed that metallic VO_2 nanodiscs can exhibit LSPRs in NIR spectrum. Combining these findings open a possibility for VO_2 nanodiscs to become an active metamaterials, whose Mie's dielectric resonances change into the plasmonic metallic resonances upon MIT. Secondly, we discussed the nature of FeRh AF-FM transition and its applications. Nanodisc fabrication process had to be adapted to negative resist,

due to an annealing process during a deposition of FeRh. With the modified EBL, we were able to produce 20 nm high FeRh nanodisc arrays with diameters varying from 140 nm to 274 nm. When measuring their optical response, we obtained LSPR resonances in the visible part of the spectrum. The observation of LSPRs in FeRh nanodiscs suggest that an interesting experiment could be performed, where the LSPR would lower the temperature required for the phase transition.

To sum up, in this thesis we obtained skills, necessary to produce nanostructures with sizes as small as 40 nm, deeper knowledge about the LSPRs and interactions between them, and skill to produce polycrystalline VO_2 in the good quality. Beside that, this thesis set the ground for at least three interesting topics — dependence of lattice resonances of nanodisc arrays on the angle of incidence, Mie's dielectric resonances in VO_2 that change into the metallic LSPRs, and LSPRs of FeRh nanodiscs as a "booster" for the phase transition of FeRh. All of them have a significant potential for research and will be further developed in future work.

List of Abbreviations

AF ..... Antiferromagnetic

AFM ..... Atomic Force Microscopy

AS ..... Aperture Stop

BF ..... Bright-field

DF ..... Dark-field

DO ..... Diffraction Order

EBL ..... Electron Beam Lithography

FDTD ..... Finite-difference Time-domain

FEBID ..... Focused Electron Beam Induced Deposition

FEBIE ..... Focused Electron Beam Induced Etching

FIB ..... Focused Ion Beam

FIBID ..... Focused Ion Beam Induced Deposition

FIBIE ..... Focused Ion Beam Induced Etching

FM ..... Ferromagnetic

GIS ..... Gas Injection System

GND ..... Gold Nanodisc

IPA ..... Isopropyl Alcohol

IR ..... Infrared

LSP ..... Localized Surface Plasmon

LSPR ..... Localized Surface Plasmon Resonance

MIR ..... Mid-infrared

MIT ..... Metal–insulator Transition

NA ..... Numerical aperture

NIR ..... Near-infrared

NP ..... Nanoparticle

SEM ..... Scanning Electron Microscope

UV ..... Ultraviolet

Bibliography

[1] Silverstone, J. W. *Entangled light in silicon waveguides*. Doctoral thesis, University of Bristol, Bristol, 2015.

[2] Gates, B. D., Xu, Q., Stewart, M., *et al.* New Approaches to Nanofabrication. *Chemical Reviews*, 105 (4), **2005**, pp. 1171–1196. DOI: 10.1021/cr030076o.

[3] Ligmajer, F. *Uspořádaná a neuspořádaná pole koloidních nanočástic a jejich využití pro detekci biomolekul*. Diplomová práce, Vysoké učení technické v Brně, Fakulta strojního inženýrství, Brno, 2013.

[4] Bhushan, B. *Springer handbook of nanotechnology*. Springer-Verlag, Berlin, [1st ed.] edn., 2004. ISBN 3-540-01218-4.

[5] Pimpin, A. and Srituravanich, W. Review on Micro- and Nanolithography Techniques and their Applications. *Engineering Journal*, 16 (1), **2012**, pp. 37–56. DOI: 10.4186/ej.2012.16.1.37.

[6] van Assenbergh, P., Meinders, E., Geraedts, J., and Dodou, D. Nanostructure and Microstructure Fabrication. *Small*, 14 (20), **2018**. DOI: 10.1002/smll.201703401.

[7] Šamořil, T. *Aplikace fokusovaného iontového a elektronového svazku v nanotechno- logiích*. Disertace, Vysoké učení technické v Brně, Fakulta strojního inženýrství, Brno, 2015.

[8] Wnuk, J., Rosenberg, S., Gorham, J., *et al.* Electron beam deposition for nanofabrication. *Surface Science*, 605 (3-4), **2011**, pp. 257–266. DOI: 10.1016/j.susc.2010.10.035.

[9] Lin, B. A comparison of projection and proximity printings —from UV to x-ray. *Microelectronic Engineering*, 11 (1-4), **1990**, pp. 137–145. DOI: 10.1016/0167-9317(90)90089-C.

[10] Manfrinato, V. R., Zhang, L., Su, D., *et al.* Resolution Limits of Electron-Beam Lithography toward the Atomic Scale. *Nano Letters*, 13 (4), **2013**, pp. 1555–1558. DOI: 10.1021/nl304715p.

[11] Ahn, J.-J., Moon, K.-S., and Koo, S.-M. Nano-structure fabrication of GaAs using AFM tip-induced local oxidation method. *Nanoscale Research Letters*, 6 (1), **2011**. DOI: 10.1186/1556-276X-6-550.

[12] Horák, M., Bukvišová, K., Švarc, V., *et al.* Comparative study of plasmonic antennas fabricated by electron beam and focused ion beam lithography. *Scientific Reports*, 8 (1), **2018**. DOI: 10.1038/s41598-018-28037-1.

[13] Utke, I., Moshkalev, S., and Russell, P. *Nanofabrication using focused ion and electron beams*. Oxford University Press, New York, 2012. ISBN 978-0-19-973421-4.

[14] Sarangan, A. *Nanofabrication*. CRC Press, Boca Raton, 1 edn., 2017. ISBN 978-149-8725-576.

[15] Babocký, J. *Tvorba plazmonických mikro a nanostruktur pomocí elektronové litografie*. Bakalářská práce, Vysoké učení technické v Brně, Fakulta strojního inženýrství, Brno, 2012.

[16] Rovenská, K. *Kovové nanostruktury s trojrozměrnou topografií pro plazmoniku*. Bakalářská práce, Vysoké učení technické v Brně, Fakulta strojního inženýrství, Brno, 2018.

[17] Zorić, I., Zäch, M., Kasemo, B., and Langhammer, C. Gold, Platinum, and Aluminum Nanodisk Plasmons. *ACS Nano*, 5 (4), **2011**, pp. 2535–2546. DOI: 10.1021/nn102166t.

[18] TESCAN. *Vega 3 SEM - Instructions For Use Manual*. Brno, 2011.

[19] Nanosuite. *Software Operation Manual*. Dortmund, 2010.

[20] Sommerfeld, A. Ueber die Fortpflanzung elektrodynamischer Wellen längs eines Drahtes. *Annalen der Physik und Chemie*, 303 (2), **1899**, pp. 233–290. DOI: 10.1002/andp.18993030202.

[21] Drude, P. Zur Elektronentheorie der Metalle. *Annalen der Physik*, 306 (3), **1900**, pp. 566–613. DOI: 10.1002/andp.19003060312.

[22] Zenneck, J. Über die Fortpflanzung ebener elektromagnetischer Wellen längs einer ebenen Leiterfläche und ihre Beziehung zur drahtlosen Telegraphie. *Annalen der Physik*, 328 (10), **1907**, pp. 846–866. DOI: 10.1002/andp.19073281003.

[23] Mubeen, S., Lee, J., ram Lee, W., *et al.* On the Plasmonic Photovoltaic. *ACS Nano*, 8 (6), **2014**, pp. 6066–6073. DOI: 10.1021/nn501379r.

[24] Brongersma, M. L., Cui, Y., and Fan, S. Light management for photovoltaics using high-index nanostructures. *Nature Materials*, 13 (5), **2014**, pp. 451–460. DOI: 10.1038/nmat3921.

[25] Boriskina, S. V., Ghasemi, H., and Chen, G. Plasmonic materials for energy. *Materials Today*, 16 (10), **2013**, pp. 375–386. DOI: 10.1016/j.mattod.2013.09.003.

[26] Atwater, H. A. and Polman, A. Plasmonics for improved photovoltaic devices. *Nature Materials*, 9 (3), **2010**, pp. 205–213. DOI: 10.1038/nmat2629.

[27] Li, W. and Valentine, J. Metamaterial Perfect Absorber Based Hot Electron Photodetection. *Nano Letters*, 14 (6), **2014**, pp. 3510–3514. DOI: 10.1021/nl501090w.

[28] Ly-Gagnon, D.-S., Balram, K. C., White, J. S., *et al.* Routing and photodetection in subwavelength plasmonic slot waveguides. *Nanophotonics*, 1 (1), **2012**. DOI: 10.1515/nanoph-2012-0002.

[29] Chalabi, H., Schoen, D., and Brongersma, M. L. Hot-Electron Photodetection with a Plasmonic Nanostripe Antenna. *Nano Letters*, 14 (3), **2014**, pp. 1374–1380. DOI: 10.1021/nl4044373.

[30] Knight, M. W., Sobhani, H., Nordlander, P., and Halas, N. J. Photodetection with Active Optical Antennas. *Science*, 332 (6030), **2011**, pp. 702–704. DOI: 10.1126/science.1203056.

[31] Rodríguez-Oliveros, R. and Sánchez-Gil, J. A. Gold nanostars as thermoplasmonic nanoparticles for optical heating. *Optics Express*, 20 (1), **2012**. DOI: 10.1364/OE.20.000621.

[32] Mutlu, M., Kang, J.-H., Raza, S., *et al.* Thermoplasmonic Ignition of Metal Nanoparticles. *Nano Letters*, 18 (3), **2018**, pp. 1699–1706. DOI: 10.1021/acs.nanolett.7b04739.

[33] Jack, C., Karimullah, A. S., Tullius, R., *et al.* Spatial control of chemical processes on nanostructures through nano-localized water heating. *Nature Communications*, 7 (1), **2016**. DOI: 10.1038/ncomms10946.

[34] Baffou, G. and Quidant, R. Thermo-plasmonics. *Laser Photonics Rev.*, 7 (2), **2013**, pp. 171–187. DOI: 10.1002/lpor.201200003.

[35] Khorasaninejad, M. and Capasso, F. Metalenses. *Science*, 358 (6367), **2017**. DOI: 10.1126/science.aam8100.

[36] Genevet, P., Capasso, F., Aieta, F., *et al.* Recent advances in planar optics. *Optica*, 4 (1), **2017**. DOI: 10.1364/OPTICA.4.000139.

[37] Yu, N., Genevet, P., Kats, M. A., *et al.* Light Propagation with Phase Discontinuities. *Science*, 334 (6054), **2011**, pp. 333–337. DOI: 10.1126/science.1210713.

[38] Hsiao, H.-H., Chu, C. H., and Tsai, D. P. Fundamentals and Applications of Metasurfaces. *Small Methods*, 1 (4), **2017**. DOI: 10.1002/smtd.201600064.

[39] Liu, Y. and Zhang, X. Metamaterials. *Chemical Society Reviews*, 40 (5), **2011**. DOI: 10.1039/c0cs00184h.

[40] Shalaev, V. M. Optical negative-index metamaterials. *Nature Photonics*, 1 (1), **2007**, pp. 41–48. DOI: 10.1038/nphoton.2006.49.

[41] Smith, D. R. Metamaterials and Negative Refractive Index. *Science*, 305 (5685), **2004-08-06**, pp. 788–792. DOI: 10.1126/science.1096796.

[42] Šípová, H. and Homola, J. Surface plasmon resonance sensing of nucleic acids. *Analytica Chimica Acta*, 773, **2013**, pp. 9–23. DOI: 10.1016/j.aca.2012.12.040.

[43] Scarano, S., Mascini, M., Turner, A. P., and Minunni, M. Surface plasmon resonance imaging for affinity-based biosensors. *Biosensors and Bioelectronics*, 25 (5), **2010**, pp. 957–966. DOI: 10.1016/j.bios.2009.08.039.

[44] Homola, J. Surface Plasmon Resonance Sensors for Detection of Chemical and Biological Species. *Chemical Reviews*, 108 (2), **2008**, pp. 462–493. DOI: 10.1021/cr068107d.

[45] Maier, S. A. *Plasmonics*. Springer,, New York, 1 edn., 2007. ISBN 978-0-387-37825-1.

[46] Sedlák, B. and Štoll, I. *Elektřina a magnetismus*. Karolinum, Praha, vyd. 3., v nakl. karolinum 2 edn., 2012. ISBN 978-80-246-2198-2.

[47] Ligmajer, F. *Pokročilé plazmonické materiály pro metapovrchy a fotochemii*. Dizertační práce, CEITEC VUT, Brno, 2018.

[48] Griffiths, D. J. *Introduction to electrodynamics*. Prentice Hall, Upper Saddle River, N.J., 3rd ed edn., 1999. ISBN 01-380-5326-X.

[49] Hanarp, P., Käll, M., and Sutherland, D. S. Optical Properties of Short Range Ordered Arrays of Nanometer Gold Disks Prepared by Colloidal Lithography. *The Journal of Physical Chemistry B*, 107 (24), **2003**, pp. 5768–5772. DOI: 10.1021/jp027562k.

[50] Langhammer, C., Yuan, Z., Zorić, I., and Kasemo, B. Plasmonic Properties of Supported Pt and Pd Nanostructures. *Nano Letters*, 6 (4), **2006**, pp. 833–838. DOI: 10.1021/nl060219x.

[51] Langhammer, C., Kasemo, B., and Zorić, I. Absorption and scattering of light by Pt, Pd, Ag, and Au nanodisks. *The Journal of Chemical Physics*, 126 (19), **2007**. DOI: 10.1063/1.2734550.

[52] Lamprecht, B., Schider, G., Lechner, R. T., *et al.* Metal Nanoparticle Gratings. *Physical Review Letters*, 84 (20), **2000**, pp. 4721–4724. DOI: 10.1103/PhysRevLett.84.4721.

[53] Haynes, C. L., McFarland, A. D., Zhao, L., *et al.* Nanoparticle Optics. *The Journal of Physical Chemistry B*, 107 (30), **2003**, pp. 7337–7342. DOI: 10.1021/jp034234r.

[54] Mie, G. Beiträge zur Optik trüber Medien, speziell kolloider Metallösungen. *Annalen der Physik*, 330 (3), **1908**, p. 377 – 445.

[55] Kalousek, R., Dub, P., Břínek, L., and Šikola, T. Response of plasmonic resonant nanorods. *Optics Express*, 20 (16), **2012**. DOI: 10.1364/OE.20.017916.

[56] Binkova, P. *Průmyslové aplikace optických nanoantén*. Bakalářská práce, Vysoké učení technické v Brně, Fakulta strojního inženýrství, Brno, 2018.

[57] Gunnarsson, L., Rindzevicius, T., Prikulis, J., *et al.* Confined Plasmons in Nanofabricated Single Silver Particle Pairs. *The Journal of Physical Chemistry B*, 109 (3), **2005**, pp. 1079–1087. DOI: 10.1021/jp049084e.

[58] Nehl, C. L., Grady, N. K., Goodrich, G. P., *et al.* Scattering Spectra of Single Gold Nanoshells. *Nano Letters*, 4 (12), **2004**, pp. 2355–2359. DOI: 10.1021/nl048610a.

[59] Hu, M., Novo, C., Funston, A., *et al.* Dark-field microscopy studies of single metal nanoparticles understanding the factors that influence the linewidth of the localized surface plasmon resonance. *Journal of Materials Chemistry*, 18 (17), **2008**. DOI: 10.1039/B714759G.

[60] Hicks, E. M., Zou, S., Schatz, G. C., *et al.* Controlling Plasmon Line Shapes through Diffractive Coupling in Linear Arrays of Cylindrical Nanoparticles Fabricated by Electron Beam Lithography. *Nano Letters*, 5 (6), **2005**, pp. 1065–1070. DOI: 10.1021/nl0505492.

[61] Harris, N., Arnold, M. D., Blaber, M. G., and Ford, M. J. Plasmonic Resonances of Closely Coupled Gold Nanosphere Chains. *The Journal of Physical Chemistry C*, 113 (7), **2009**, pp. 2784–2791. DOI: 10.1021/jp8083869.

[62] Aigouy, L., Prieto, P., Vitrey, A., *et al.* Strong near-field optical localization on an array of gold nanodisks. *Journal of Applied Physics*, 110 (4), **2011**. DOI: 10.1063/1.3624749.

[63] Encina, E. R. and Coronado, E. A. Plasmon Coupling in Silver Nanosphere Pairs. *The Journal of Physical Chemistry C*, 114 (9), **2010**, pp. 3918–3923. DOI: 10.1021/jp912096v.

[64] Sung, J., Hicks, E. M., Duyne, R. P. V., and Spears, K. G. Nanoparticle Spectroscopy. *The Journal of Physical Chemistry C*, 112 (11), **2008**, pp. 4091–4096. DOI: 10.1021/jp077332b.

[65] Chu, Y., Schonbrun, E., Yang, T., and Crozier, K. B. Experimental observation of narrow surface plasmon resonances in gold nanoparticle arrays. *Applied Physics Letters*, 93 (18), **2008**. DOI: 10.1063/1.3012365.

[66] Auguié, B. and Barnes, W. L. Collective Resonances in Gold Nanoparticle Arrays. *Physical Review Letters*, 101 (14), **2008**. DOI: 10.1103/PhysRevLett.101.143902.

[67] Esposito, M., Todisco, F., Bakhti, S., *et al.* Symmetry Breaking in Oligomer Surface Plasmon Lattice Resonances. *Nano Letters*, 19 (3), **2019**, pp. 1922–1930. DOI: 10.1021/acs.nanolett.8b05062.

[68] Raoux, S. Phase Change Materials. *Annual Review of Materials Research*, 39 (1), **2009**, pp. 25–48. DOI: 10.1146/annurev-matsci-082908-145405.

[69] Wang, J.-J., Xu, Y.-Z., Mazzarello, R., *et al.* A Review on Disorder-Driven Metal–Insulator Transition in Crystalline Vacancy-Rich GeSbTe Phase-Change Materials. *Materials*, 10 (8), **2017**. DOI: 10.3390/ma10080862.

[70] Maat, S., Thiele, J. U., and Fullerton, E. E. Temperature and field hysteresis of the antiferromagnetic to ferromagnetic phase transition in epitaxial FeRh films. *Physical Review B*, 72 (21), **2005**. DOI: 10.1103/PhysRevB.72.214432.

[71] Wang, Q., Rogers, E. T. F., Gholipour, B., *et al.* Optically reconfigurable metasurfaces and photonic devices based on phase change materials. *Nature Photonics*, 10 (1), **2016**, pp. 60–65. DOI: 10.1038/nphoton.2015.247.

[72] Zhang, W., Mazzarello, R., Wuttig, M., and Ma, E. Designing crystallization in phase-change materials for universal memory and neuro-inspired computing. *Nature Reviews Materials*, 4 (3), **2019**, pp. 150–168. DOI: 10.1038/s41578-018-0076-x.

[73] Wuttig, M. and Yamada, N. Phase-change materials for rewriteable data storage. *Nature Materials*, 6 (11), **2007**, pp. 824–832. DOI: 10.1038/nmat2009.

[74] Morin, F. J. Oxides Which Show a Metal-to-Insulator Transition at the Neel Temperature. *Physical Review Letters*, 3 (1), **1959**, pp. 34–36. DOI: 10.1103/PhysRevLett.3.34.

[75] Yang, Z., Ko, C., and Ramanathan, S. Oxide Electronics Utilizing Ultrafast Metal-Insulator Transitions. *Annual Review of Materials Research*, 41 (1), **2011**, pp. 337–367. DOI: 10.1146/annurev-matsci-062910-100347.

[76] Nag, J. *The Solid-solid Phase Transition in Vanadium Dioxide Thin Films*. Doctoral thesis, Faculty of the Graduate School of Vanderbilt University, Nashville, Tennessee, 2011.

[77] Tselev, A., Luk'yanchuk, I. A., Ivanov, I. N., *et al.* Symmetry Relationship and Strain-Induced Transitions between Insulating M1 and M2 and Metallic R phases of Vanadium Dioxide. *Nano Letters*, 10 (11), **2010**, pp. 4409–4416. DOI: 10.1021/nl1020443.

[78] Huffman, T. J., Hendriks, C., Walter, E. J., *et al.* Insulating phases of vanadium dioxide are Mott-Hubbard insulators. *Physical Review B*, 95 (7), **2017**. DOI: 10.1103/PhysRevB.95.075125.

[79] Appavoo, K. *Hybrid Phase-Changing Nanostructures*. Doctoral thesis, Faculty of the Graduate School of Vanderbilt University, Nashville, Tennessee, 2012.

[80] Walden, R. Two switching devices utilizing VO 2. *IEEE Transactions on Electron Devices*, 17 (8), **1970**, pp. 603–612. DOI: 10.1109/T-ED.1970.17037.

[81] Manning, T. D., Parkin, I. P., Clark, R. J. H., *et al.* Intelligent window coatings. *Journal of Materials Chemistry*, 12 (10), **2002**, pp. 2936–2939. DOI: 10.1039/b205427m.

[82] Kim, B.-J., Lee, Y. W., Chae, B.-G., *et al.* Temperature dependence of the first-order metal-insulator transition in VO2 and programmable critical temperature sensor. *Applied Physics Letters*, 90 (2), **2007**. DOI: 10.1063/1.2431456.

[83] Chivian, J., Scott, M., Case, W., and Krasutsky, N. An improved scan laser with a VO 2 programmable mirror. *IEEE Journal of Quantum Electronics*, 21 (4), **1985**, pp. 383–390. DOI: 10.1109/JQE.1985.1072656.

[84] Roach, W. R. Holographic Storage in VO 2. *Applied Physics Letters*, 19 (11), **1971**, pp. 453–455. DOI: 10.1063/1.1653769.

[85] Jin, P., Tazawa, M., and Xu, G. Reversible tuning of surface plasmon resonance of silver nanoparticles using a thermochromic matrix. *Journal of Applied Physics*, 99 (9), **2006**. DOI: 10.1063/1.2193336.

[86] Earl, S. K., James, T. D., Gómez, D. E., *et al.* Switchable polarization rotation of visible light using a plasmonic metasurface. *APL Photonics*, 2 (1), **2017**. DOI: 10.1063/1.4968840.

[87] Appavoo, K., Wang, B., Brady, N. F., *et al.* Ultrafast Phase Transition via Catastrophic Phonon Collapse Driven by Plasmonic Hot-Electron Injection. *Nano Letters*, 14 (3), **2014**, pp. 1127–1133. DOI: 10.1021/nl4044828.

[88] Marvel, R. E., Harl, R. R., Craciun, V., *et al.* Influence of deposition process and substrate on the phase transition of vanadium dioxide thin films. *Acta Materialia*, 91, **2015**, pp. 217–226. DOI: 10.1016/j.actamat.2015.03.009.

[89] Marvel, R. E., Appavoo, K., Choi, B. K., *et al.* Electron-beam deposition of vanadium dioxide thin films. *Applied Physics A*, 111 (3), **2013**, pp. 975–981. DOI: 10.1007/s00339-012-7324-5.

[90] Lee, S., Meyer, T. L., Park, S., *et al.* Growth control of the oxidation state in vanadium oxide thin films. *Applied Physics Letters*, 105 (22), **2014**. DOI: 10.1063/1.4903348.

[91] Ligmajer, F., Kejík, L., Tiwari, U., *et al.* Epitaxial VO 2 Nanostructures. *ACS Photonics*, 5 (7), **2017**, pp. 2561–2567. DOI: 10.1021/acsphotonics.7b01384.

[92] Suh, J. Y., Lopez, R., Feldman, L. C., and Haglund, R. F. Semiconductor to metal phase transition in the nucleation and growth of VO2 nanoparticles and thin films. *Journal of Applied Physics*, 96 (2), **2004**, pp. 1209–1213. DOI: 10.1063/1.1762995.

[93] Jahani, S. and Jacob, Z. All-dielectric metamaterials. *Nature Nanotechnology*, 11 (1), **2016**, pp. 23–36. DOI: 10.1038/nnano.2015.304.

[94] Kuznetsov, A. I., Miroshnichenko, A. E., Brongersma, M. L., *et al.* Optically resonant dielectric nanostructures. *Science*, 354 (6314), **2016**. DOI: 10.1126/science.aag2472.

[95] Kouvel, J. S. and Hartelius, C. C. Anomalous Magnetic Moments and Transformations in the Ordered Alloy FeRh. *Journal of Applied Physics*, 33 (3), **1962**, pp. 1343–1344. DOI: 10.1063/1.1728721.

[96] Uhlíř, V., Arregi, J. A., and Fullerton, E. E. Colossal magnetic phase transition asymmetry in mesoscale FeRh stripes. *Nature Communications*, 7 (1), **2016**. DOI: 10.1038/ncomms13113.

[97] Annaorazov, M. P., Nikitin, S. A., Tyurin, A. L., *et al.* Anomalously high entropy change in FeRh alloy. *Journal of Applied Physics*, 79 (3), **1996**, pp. 1689–1695. DOI: 10.1063/1.360955.

[98] Thiele, J.-U., Maat, S., and Fullerton, E. E. FeRh/FePt exchange spring films for thermally assisted magnetic recording media. *Applied Physics Letters*, 82 (17), **2003**, pp. 2859–2861. DOI: 10.1063/1.1571232.

[99] Marti, X., Fina, I., Frontera, C., *et al.* Room-temperature antiferromagnetic memory resistor. *Nature Materials*, 13 (4), **2014**, pp. 367–374. DOI: 10.1038/nmat3861.

[100] Mariager, S. O., Pressacco, F., Ingold, G., *et al.* Structural and Magnetic Dynamics of a Laser Induced Phase Transition in FeRh. *Physical Review Letters*, 108 (8), **2012**. DOI: 10.1103/PhysRevLett.108.087201.